



# **NAVAL POSTGRADUATE SCHOOL**

**MONTEREY, CALIFORNIA**

## **THESIS**

### **ROUGHNESS LENGTH VARIABILITY OVER HETEROGENEOUS SURFACES**

by

Matthew A. Ellis

March 2010

Thesis Advisor:  
Second Reader:

Qing Wang  
Wendell A. Nuss

**Approved for public release; distribution is unlimited**

<b>REPORT DOCUMENTATION PAGE</b>			<i>Form Approved OMB No. 0704-0188</i>	
Public reporting burden for this collection of information is estimated to average 1 hour per response, including the time for reviewing instruction, searching existing data sources, gathering and maintaining the data needed, and completing and reviewing the collection of information. Send comments regarding this burden estimate or any other aspect of this collection of information, including suggestions for reducing this burden, to Washington headquarters Services, Directorate for Information Operations and Reports, 1215 Jefferson Davis Highway, Suite 1204, Arlington, VA 22202-4302, and to the Office of Management and Budget, Paperwork Reduction Project (0704-0188) Washington DC 20503.				
<b>1. AGENCY USE ONLY (Leave blank)</b>		<b>2. REPORT DATE</b> March 2010	<b>3. REPORT TYPE AND DATES COVERED</b> Master's Thesis	
<b>4. TITLE AND SUBTITLE</b> Roughness Length Variability over Heterogeneous Surfaces			<b>5. FUNDING NUMBERS</b>	
<b>6. AUTHOR(S)</b> Matthew A. Ellis			<b>8. PERFORMING ORGANIZATION REPORT NUMBER</b>	
<b>7. PERFORMING ORGANIZATION NAME(S) AND ADDRESS(ES)</b> Naval Postgraduate School Monterey, CA 93943-5000			<b>10. SPONSORING/MONITORING AGENCY REPORT NUMBER</b>	
<b>9. SPONSORING /MONITORING AGENCY NAME(S) AND ADDRESS(ES)</b> N/A			<b>10. SPONSORING/MONITORING AGENCY REPORT NUMBER</b>	
<b>11. SUPPLEMENTARY NOTES</b> The views expressed in this thesis are those of the author and do not reflect the official policy or position of the Department of Defense or the U.S. Government. IRB Protocol Number _____				
<b>12a. DISTRIBUTION / AVAILABILITY STATEMENT</b> Approved for public release; distribution is unlimited			<b>12b. DISTRIBUTION CODE</b>	
<b>13. ABSTRACT</b> Monin-Obukhov similarity theory and the empirical formulae of Businger et al. (1971) and Dyer (1974) are used to calculate roughness lengths and surface-layer heat fluxes from multilevel observations of wind, temperature, and humidity measured at three locations in the Weather Information Network Display System at Cape Canaveral Air Force Station, Florida. Relationships between roughness length and surface-layer wind speed and direction in varying thermal stability conditions are analyzed during two four-day periods: a diurnally-cycling coastal wind circulation regime on 1–4 June 2008 and the passage of Tropical Storm Fay on 18–21 August 2008. Spatial and temporal variations in roughness lengths for a period of one year are compared to landscape features near the three observation platforms using shadow analysis of satellite photographs. Wind speeds during the coastal wind event remained below 10 ms <sup>-1</sup> , and roughness lengths calculated from observations below 60 m corresponded to surface roughness elements within about 300 m. At the same height in the tropical storm case, for wind speeds exceeding 20 ms <sup>-1</sup> , evidence is presented that indicates roughness lengths are related to surface features up to 1.5 km upstream.				
<b>14. SUBJECT TERMS</b> Atmospheric Boundary Layer, Turbulence, Roughness Length, Momentum Flux, Heat Flux, Flux-Profile Relationships, Monin-Obukhov Similarity Theory, Heterogeneous Surfaces			<b>15. NUMBER OF PAGES</b> 97	
			<b>16. PRICE CODE</b>	
<b>17. SECURITY CLASSIFICATION OF REPORT</b> Unclassified	<b>18. SECURITY CLASSIFICATION OF THIS PAGE</b> Unclassified	<b>19. SECURITY CLASSIFICATION OF ABSTRACT</b> Unclassified	<b>20. LIMITATION OF ABSTRACT</b> UU	

NSN 7540-01-280-5500

Standard Form 298 (Rev. 8-98)  
Prescribed by ANSI Std. Z39.18

THIS PAGE INTENTIONALLY LEFT BLANK

**Approved for public release; distribution is unlimited**

**ROUGHNESS LENGTH VARIABILITY OVER HETEROGENEOUS SURFACES**

Matthew A. Ellis  
Captain, United States Air Force  
B.S., The Florida State University – Tallahassee, 2003

Submitted in partial fulfillment of the  
requirements for the degree of

**MASTER OF SCIENCE IN METEOROLOGY**

from the

**NAVAL POSTGRADUATE SCHOOL  
March 2010**

Author: Matthew A. Ellis

Approved by: Qing Wang  
Thesis Advisor

Wendell A. Nuss  
Second Reader

Philip A. Durkee  
Chair, Department of Meteorology

THIS PAGE INTENTIONALLY LEFT BLANK

## ABSTRACT

Monin-Obukhov similarity theory and the empirical formulae of Businger et al. (1971) and Dyer (1974) are used to calculate roughness lengths and surface-layer heat fluxes from multilevel observations of wind, temperature, and humidity measured at three locations in the Weather Information Network Display System at Cape Canaveral Air Force Station, Florida. Relationships between roughness length and surface-layer wind speed and direction in varying thermal stability conditions are analyzed during two four-day periods: a diurnally-cycling coastal wind circulation regime on 1–4 June 2008 and the passage of Tropical Storm Fay on 18–21 August 2008. Spatial and temporal variations in roughness lengths for a period of one year are compared to landscape features near the three observation platforms using shadow analysis of satellite photographs. Wind speeds during the coastal wind event remained below  $10 \text{ ms}^{-1}$ , and roughness lengths calculated from observations below 60 m corresponded to surface roughness elements within about 300 m. At the same height in the tropical storm case, for wind speeds exceeding  $20 \text{ ms}^{-1}$ , evidence is presented that indicates roughness lengths are related to surface features up to 1.5 km upstream.

THIS PAGE INTENTIONALLY LEFT BLANK

# TABLE OF CONTENTS

I.	INTRODUCTION AND PURPOSE .....	1
A.	THE ATMOSPHERIC BOUNDARY LAYER .....	2
B.	ABL PARAMETERIZATION IN NUMERICAL MODELS.....	3
1.	Turbulent Transport .....	3
2.	Roughness Length .....	4
a.	<i>Definition and Measurement Methods</i> .....	4
b.	<i>Roughness Length in Numerical Models</i> .....	6
3.	Internal Boundary Layers over Heterogeneous Surfaces ....	7
4.	Surface Flux Parameterization over Heterogeneous Surfaces .....	8
C.	PURPOSE AND OVERVIEW OF THESIS .....	9
D.	MILITARY APPLICATIONS.....	10
II.	SURFACE-LAYER THERMODYNAMICS .....	11
A.	TURBULENT TRANSPORT .....	11
B.	SURFACE-LAYER SCALING PARAMETERS AND FLUXES .....	12
C.	SURFACE-LAYER FLUX-PROFILE RELATIONSHIPS.....	14
D.	BULK AERODYNAMIC PARAMETERIZATIONS .....	19
III.	OBSERVATIONS AND SELECTED CASES .....	21
A.	SURFACE-LAYER OBSERVATIONS .....	21
1.	Launch Critical Towers .....	22
2.	Safety Critical Towers .....	23
3.	Forecast Critical Towers .....	24
4.	Data Processing.....	24
B.	CASES SELECTED FOR THIS STUDY .....	28
1.	Surface Morphology .....	28
2.	Coastal Wind Circulations .....	29
3.	Tropical Storm Fay .....	31
IV.	RESULTS AND ANALYSES .....	37
A.	ROUGHNESS LENGTH VARIATION IN RESPONSE TO COASTAL WIND CIRCULATIONS.....	37
1.	Tower 0006 .....	37
2.	Tower 0110 .....	43
B.	ROUGHNESS LENGTH VARIATION IN RESPONSE TO TROPICAL STORM FAY .....	49
1.	Tower 0002 .....	49
2.	Tower 0110 .....	57
C.	ROUGHNESS LENGTH FROM DIFFERENT OBSERVATION LEVELS .....	63
V.	CONCLUSION .....	67
A.	SUMMARY OF RESULTS .....	67



B.	RECOMMENDATIONS FOR FUTURE RESEARCH USING THE WINDS OBSERVATIONS.....	70
APPENDIX.	WINDS TOWER LOCATIONS AND INSTRUMENT COMPLEMENTS .....	71
	LIST OF REFERENCES.....	73
	INITIAL DISTRIBUTION LIST .....	77

## LIST OF FIGURES

Figure 1.	Typical roughness lengths arranged by surface type. From Stull (1988).....	5
Figure 2.	Diagram of an internal boundary layer. From Stull (1988). ....	8
Figure 3.	WINDS tower distribution on and near CCAFS on the Atlantic Coast of Florida. After CSR (2006). ....	22
Figure 4.	Photograph of the upper levels of Tower 0313, a 150-m launch critical mast. Note the dual instrumentation on horizontal supports at each level. From CSR (2006). ....	23
Figure 5.	Photograph of a typical safety critical tower. From CSR (2006). ....	24
Figure 6.	Temporal variation of observed (a) absolute virtual potential temperature ( $\theta_v$ ) and (b) specific humidity ( $q$ ) in $\text{g kg}^{-1}$ and calculated (c) sensible and (d) latent heat fluxes in $\text{Wm}^{-2}$ from the northeast sensors at temperature levels 1 and 2 of Tower 0313 on 2–5 May 2008.....	26
Figure 7.	Temporal variation of observed (a) wind speed (WS) in $\text{ms}^{-1}$ and (b) wind direction (WD) in degrees and calculated (c) roughness length ( $z_0$ ) in m and (d) friction velocity ( $u_*$ ) in $\text{ms}^{-1}$ from the northeast sensors at wind levels 1 and 2 of Tower 0313 on 2–5 May 2008. ....	27
Figure 8.	Vertical variation of observed (a) virtual potential temperature ( $\theta_v$ ), (b) specific humidity ( $q$ ), (c) wind speed (WS), and (d) wind direction (WD) from the northeast sensors of Tower 0313 on 4 May 2008. ....	31
Figure 9.	Track of the center of Tropical Storm Fay. From Stewart and Beven (2009).....	32
Figure 10.	Same as Figure 6, except observed conditions and calculated quantities are from the southeast sensors at temperature levels 1 and 2 of Tower 0006 on 18–21 August 2008.....	33
Figure 11.	Same as Figure 7, except observed conditions and calculated quantities are from the southeast sensors at wind levels 1 and 2 of Tower 0006 on 18–21 August 2008.....	34
Figure 12.	Same as Figure 8, except observed conditions are from the southeast sensors of Tower 0006 on 20 August 2008.....	35
Figure 13.	Satellite photograph of Tower 0006 and surrounding area. Red "X" marks the tower location. In all satellite photographs presented herein, true north, or $360^\circ$ , is oriented toward the top of the image. Image ©2010 Google. ....	38
Figure 14.	Satellite photograph of Tower 0006 and immediate surroundings. Red "X" marks the tower location. Image ©2010 Google. ....	38
Figure 15.	Same as Figure 6, except observed conditions and calculated quantities are from the southeast sensors at temperature levels 1 and 2 of Tower 0006 on 1–4 June 2008.....	40

Figure 16.	Same as Figure 7, except observed conditions and calculated quantities are from the southeast sensors at wind levels 1 and 2 of Tower 0006 on 1–4 June 2008.....	40
Figure 17.	Same as Figure 7, except observed conditions and calculated quantities are from the southeast sensors at wind levels 2 and 3 of Tower 0006 on 1–4 June 2008.....	41
Figure 18.	Azimuthal variation of calculated roughness length $z_0$ averaged over each 15° sector from the southeast sensors at (a) wind levels 1 and 2 and (b) wind levels 2 and 3 of Tower 0006 for 1 January to 31 December 2008.....	43
Figure 19.	Satellite photograph of Tower 0110 and surrounding area. Red "X" marks the tower location. Image ©2010 Google.....	44
Figure 20.	Satellite photograph of Tower 0110 and immediate surroundings. Red "X" marks the tower location. Image ©2010 Google. ....	45
Figure 21.	Same as Figure 6, except observed conditions and calculated quantities are from the southeast sensors at temperature levels 1 and 2 of Tower 0110 on 1–4 June 2008.....	46
Figure 22.	Same as Figure 7, except observed conditions and calculated quantities are from the southeast sensors at wind levels 1 and 2 of Tower 0110 on 1–4 June 2008.....	47
Figure 23.	Same as Figure 7, except observed conditions and calculated quantities are from the southeast sensors at wind levels 2 and 3 of Tower 0110 on 1–4 June 2008.....	48
Figure 24.	Azimuthal variation of calculated roughness length $z_0$ averaged over each 15° sector from the southeast sensors at (a) wind levels 1 and 2 and (b) wind levels 2 and 3 of Tower 0110 for 1 January to 31 December 2008.....	49
Figure 25.	Satellite photograph of Tower 0002 and surrounding area. Red "X" marks the tower location. Image ©2010 Google.....	50
Figure 26.	Satellite photograph of Tower 0002 and immediate surroundings. Red "X" marks the tower location. Image ©2010 Google. ....	50
Figure 27.	Same as Figure 6, except observed conditions and calculated quantities are from the southeast sensors at temperature levels 1 and 2 of Tower 0002 on 18–21 August 2008.....	51
Figure 28.	Same as Figure 7, except observed conditions and calculated quantities are from the southeast sensors at wind levels 1 and 2 of Tower 0002 on 18–21 August 2008.....	52
Figure 29.	Same as Figure 7, except observed conditions and calculated quantities are from the southeast sensors at wind levels 2 and 3 of Tower 0002 on 18–21 August 2008.....	53
Figure 30.	Same as Figure 6, except observed conditions and calculated quantities are from the southeast sensors at temperature levels 2 and 3 of Tower 0002 on 18–21 August 2008.....	55

Figure 31.	Same as Figure 7, except observed conditions and calculated quantities are from the southeast sensors at wind levels 4 and 5 of Tower 0002 on 18-21 August 2008. ....	56
Figure 32.	Satellite photograph showing the proximity of Tower 0002 to the Atlantic Ocean. The tower is less than 1 km from the ocean in sector 120°–180°. Red "X" marks the tower location. Image ©2010 Google.....	56
Figure 33.	Azimuthal variation of calculated roughness length $z_0$ averaged over each 15° sector from the southeast sensors at (a) wind levels 1 and 2 and (b) wind levels 2 and 3 of Tower 0002 for 1 January to 31 December 2008.....	57
Figure 34.	Same as Figure 6, except observed conditions and calculated quantities are from the southeast sensors at temperature levels 1 and 2 of Tower 0110 on 18–21 August 2008.....	58
Figure 35.	Same as Figure 7, except observed conditions and calculated quantities are from the southeast sensors at wind levels 1 and 2 of Tower 0110 on 18–21 August 2008.....	59
Figure 36.	Same as Figure 7, except observed conditions and calculated quantities are from the southeast sensors at wind levels 2 and 3 of Tower 0110 on 18–21 August 2008.....	60
Figure 37.	Satellite photograph showing the proximity of Tower 0110 to the Banana River and Atlantic Ocean. Red "X" marks the tower location. Image ©2010 Google.....	60
Figure 38.	Same as Figure 6, except observed conditions and calculated quantities are from the southeast sensors at temperature levels 2 and 3 of Tower 0110 on 18–21 August 2008.....	62
Figure 39.	Same as Figure 7, except observed conditions and calculated quantities are from the southeast sensors at wind levels 3 and 4 of Tower 0110 on 18–21 August 2008.....	63
Figure 40.	Temporal variation of observed (a) wind speed and (b) wind direction from the northwest sensors at wind levels 1 and 2 of Tower 0002 on 23–25 September 2008. ....	64
Figure 41.	Temporal variation of calculated roughness lengths at various combinations of level pairs from (a) the southeast sensors and (b) the northwest sensors of Tower 0002 on 23–25 September 2008. ....	65
Figure 42.	Contoured roughness length from (a) COAMPS and 16.5-m wind observations and calculated $z_0$ from the WINDS at (b) 0000 EST and (c) 1800 EST on 20 August 2008. COAMPS data courtesy of the Naval Research Laboratory; image ©2010 Google. ....	68

THIS PAGE INTENTIONALLY LEFT BLANK

## LIST OF TABLES

Table 1.	Locations and instrumentation heights for the four launch critical WINDS towers at CCAFS used in this study. After CSR (2006). .....	71
Table 2.	Locations and instrumentation heights for the 14 safety critical WINDS towers at CCAFS used in this study. After CSR (2006). .....	72

THIS PAGE INTENTIONALLY LEFT BLANK

## LIST OF ACRONYMS AND ABBREVIATIONS

ABL	Atmospheric Boundary Layer
AGL	(Elevation) Above Ground Level
CCAFS	Cape Canaveral Air Force Station
CSR	Computer Sciences Raytheon
EST	Eastern Standard Time
F	Fahrenheit
IBL	Internal Boundary Layer
MSL	(Elevation above) Mean Sea Level
NASA	National Aeronautics and Space Administration
NPS	Naval Postgraduate School
RH	Relative Humidity
SI	<i>Système International d'unités</i> [International System of Units]
SBF	Sea-breeze Front
TKE	Turbulence Kinetic Energy
WINDS	Weather Information Network Display System
WMO	World Meteorological Organization



THIS PAGE INTENTIONALLY LEFT BLANK

## **ACKNOWLEDGMENTS**

The author wishes to acknowledge Professor Qing Wang of the Meteorology Department at the Naval Postgraduate School (NPS). Without her expertise and patience, this thesis could not have been completed.

Additionally, my sincere gratitude is extended to visiting Professor Kostantinos Rados for his tireless efforts to develop and refine MATLAB code and to Professor Wendell A. Nuss of the NPS Meteorology Department for his insightful edits.

This thesis is dedicated to my late mother, Virginia Irene Ellis (1934–2009), who taught me the value of persistence; and to my sister, Teri Kay Hausner, who instilled in me an inquisitive mind.

THIS PAGE INTENTIONALLY LEFT BLANK

## I. INTRODUCTION AND PURPOSE

To my mind, there are two great unexplained mysteries in our understanding of the universe. One is the nature of a unified general field theory to explain both gravitation and electromagnetism. The other is an understanding of the nature of turbulence. After I die, I expect God to clarify general field theory for me. I have no such hope for turbulence. (Brown 1991)

This quotation rather elegantly expresses the complex problem of turbulence in fluid flows, though its origin is a matter of considerable speculation. Variously attributed to the Hungarian-American aerodynamicist Theodore von Kármán, the British mathematician Horace Lamb, and the German theoretical physicist Werner Heisenberg, it remains fundamentally appropriate some half century after its initial pronouncement despite decades of advances in both quantum physics and fluid dynamics.

In the classical application of Newton's second law to wave dynamics, strictly nonlinear interactions between perturbations in the flow are trivially small compared to other forcing terms and are usually neglected (Stull 1988; Holton 2004). It is precisely these nonlinear terms, however, that define the essential mechanics of turbulence in fluid flows. Given the mathematical difficulty the inclusion of higher-order nonlinearities imparts to the rigorous theoretical treatment of turbulence, numerical simulation of turbulent flow is thus dependent to some extent upon decades of empirical studies consisting of both *in situ* experimentation and computer modeling endeavors. Such studies have yielded numerous techniques for parameterizing the bulk exchanges of mass (including water and solid constituents), momentum, and energy between the Earth's surface and the atmosphere (Stewart 1979).

Although the ubiquitous Navier-Stokes and mass continuity equations theoretically describe the physics of turbulence, its complex effects elude expression in explicit detail due to the inherent nonlinearities associated with turbulent flow. In the particular case of the Earth's atmosphere, turbulence

imposes apparent randomness on the fields of mass, momentum, and energy; and the resulting system evolves chaotically in time and space. Given the formidable problem of not only characterizing the initial state and boundary conditions for turbulence, but also developing methods to iterate its evolution, the treatment of turbulence in numerical weather prediction has historically taken a stochastic approach (Lenschow 1986). In this thesis, one characteristic of turbulence in the lower atmosphere—the roughness length—is calculated using observations over heterogeneous surfaces and correlated to the physical properties of landscapes near the observation site. To facilitate this study, a brief discussion of useful terminology and concepts follows.

## **A. THE ATMOSPHERIC BOUNDARY LAYER**

The portion of the lower atmosphere extending vertically from the Earth's surface to a variable height between 100 m and 3 km comprises the *atmospheric boundary layer* (ABL) (Stull 1988); so called because it loosely defines the fluid boundary between the nongaseous surface of the planet and the remainder of the atmosphere (hereinafter the *free atmosphere*). More precisely, the generally accepted qualitative definition of the ABL is that portion of the troposphere recently in close proximity to the Earth's surface whose internal flow characteristics respond to forcing from surface features on time scales of up to one hour. In the foregoing sentence, the word *recently* implies “within approximately the previous day,” to acknowledge the dominance of the diurnal cycle on physical processes within the ABL (Stewart 1979).

The ABL contains several component layers distinguishable by their physical properties. Closest to the surface, usually extending no higher than a few centimeters in depth is the *interfacial*, or *viscous layer*. It is only in this thin envelope of air most directly in contact with the surface that transport of physical fields via turbulence is less efficient than by molecular transport (Stull 1988). Above the interfacial layer, the lowest 10% to 15% (by height) of the ABL is called the *surface*, or *constant flux layer*. In this layer, fluxes of momentum and

energy are approximately constant in the vertical, and variations in the wind field are most directly attributable to static stability and local frictional effects. The influence of the Earth's rotation is insignificant and often neglected in the surface layer (Kaimal and Finnigan 1994).

The *outer*, or *Ekman layer* comprises the bulk (about 90% by depth) of the ABL. Flow in the outer layer usually exhibits less variability in both direction and speed than in the surface layer, hence the Coriolis effect becomes a necessary consideration (Stull 1988). Moreover, in the outer layer, fluxes of energy and momentum may vary significantly with height. If sufficient lift and water vapor is present, cumuliiform clouds may develop in this layer, which alter the thermodynamic response of the entire ABL (Wang 2009). The *entrainment zone* divides the ABL from the free atmosphere. With few exceptions, this layer defines the upper boundary for turbulence generated in the ABL. The high static stability of this layer often results in a thermal inversion, characterized by an increase in temperature with height.

## **B. ABL PARAMETERIZATION IN NUMERICAL MODELS**

### **1. Turbulent Transport**

Recent advances in supercomputing technology have ushered in an era of atmospheric modeling on ever-smaller domains and at finer spatial and temporal resolutions. It has become routine practice for researchers studying microscale phenomena such as sea breezes and convective storms to employ dynamical models with grid points spaced less than 1 km (Kalnay 2003; Rao and Fuelberg 2000). Such scales are dimensionally comparable to the largest turbulent structures in the lower atmosphere; therefore, selecting optimal methods of characterizing the complex thermodynamic adjustments caused by turbulence becomes increasingly important at these resolutions. It is also readily apparent that turbulent transport of fields of meteorological interest occurs on length scales that are much smaller than 1 km (Kalnay 2003). To account for these subgrid-scale processes, modelers usually parameterize their net effect at the resolution

of the model. Researchers have developed numerous schemes for parameterizing subgrid-scale processes in the atmosphere, and this is an area of ongoing research. Ideally, as our understanding of processes associated with atmospheric turbulence continues to improve, so will our skill in accurately simulating these processes in numerical models.

## **2. Roughness Length**

### ***a. Definition and Measurement Methods***

Aerodynamic *roughness length*, frequently denoted in the literature by  $z_0$ , is the height above the local solid or liquid surface at which the velocity of the mean wind is zero (Stull 1988). By this definition, roughness length, although defined at a specific point, substantially depends upon the morphology of the surface in some neighborhood surrounding that point. Surfaces with taller, irregularly spaced individual roughness elements (trees, buildings, etc.) generally induce larger turbulent structures and thus have a larger  $z_0$ , while relatively flat surfaces scarcely disturb the flow and correspond to smaller  $z_0$ . Through decades of experimental work, over various types of land surfaces, ABL researchers established tables of roughness lengths arranged according to land use categories (Figure 1).

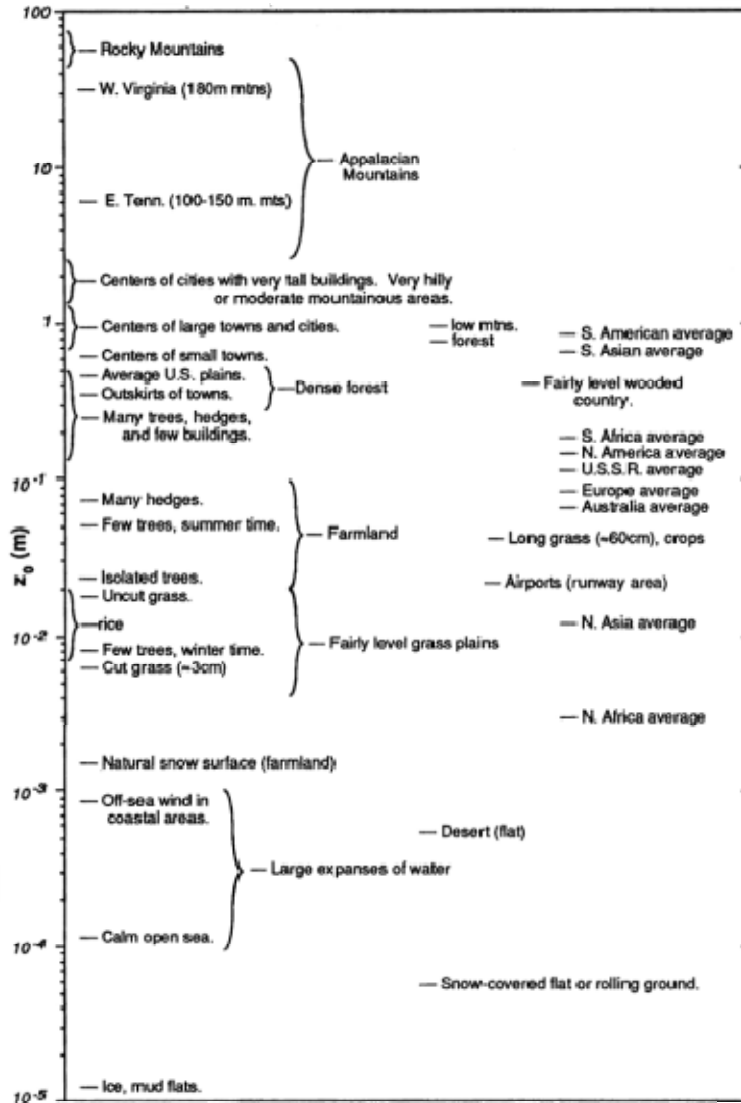


Figure 1. Typical roughness lengths arranged by surface type. From Stull (1988).

According to de Rooy and Kok (2004), the influence of variable roughness reaches its maximum at the height of local  $z_0$  and vanishes at the so-called blending height (Wieringa 1976, 1986). The experimental work of Wieringa (1986) and Caton (1977) suggests that over various surfaces, the influence of roughness elements is appreciable up to about 3 km downstream and over a 20° to 30° sector. In addition, Wieringa points out that noticeable variation in downstream gustiness often occurs on a seasonal cycle, presumably a consequence of variable foliation.



Roughness over the open ocean and large lakes varies with wave height. Charnock (1955) established the empirical expression that relates surface wind stress to wave-induced roughness. As wind stress increases, ocean waves grow higher, consequently roughness length increases. In this expression,

$$z_0 = \alpha \frac{u_*^2}{g}, \quad (1)$$

$u_*$  (introduced in Chapter II) and  $z_0$  have their customary interpretation,  $g$  is the acceleration due to gravity at the surface of the ocean, and the dimensionless  $\alpha$ , known as the Charnock parameter, has the experimentally determined value  $\alpha \approx 0.0144$ , though research suggests  $\alpha$  also has a dependence on sea state (Komen et al. 1998).

#### ***b. Roughness Length in Numerical Models***

Successful prediction of the near-surface wind field in numerical models is contingent upon accurately characterizing—either explicitly, or more commonly, by means of one or more parameterization schemes—the variation in fluxes of momentum between the atmosphere and the Earth's surface. Since surface frictional stress is a primary sink for atmospheric momentum (Newton 1971), accurate parameterizations of surface roughness improve model verification throughout the entire atmosphere. Roughness length, like many other subgrid-scale processes, is typically averaged over some finite portion of the model domain, such as the area contained in one grid box (Kalnay 2003). However, observations of low-level dynamic fields, particularly wind, often reveal strong dependences on local surface features on scales far below the resolution of the model. Modelers regard this discrepancy between observed and forecasted values, or *representation mismatch*, as part of the inherent error of the model. Jacobs and Maat (2005) stated that for the 10-m wind field, this primary

source of this error is the difference between the actual surface roughness and that used in the model's parameterization scheme.

Currently, numerical weather prediction models incorporate surface roughness as a fixed parameter for each grid point in numerical weather prediction models (Wang 2009). Such a simplistic treatment may be appropriate when modeling the slowly varying distribution or characteristics of surface roughness elements, (e.g., land use changes or seasonal variations in leaf volume or snow cover). However, research conducted by compiling and analyzing observational data presented herein suggests that such simplification may be unsatisfactory in all cases. Specifically, if roughness length were determined empirically at a grid point near the boundary between regions having different roughness characteristics, such as along a coastline or at the edge of an urban area, it is reasonable to expect that different values would be derived if the near-surface wind changed direction. If the upstream surface were smoother, it would induce smaller turbulent structures in the flow, which should contribute to an effective decrease in roughness length at the point of measurement. If at the same point, the wind were to change direction such that air passing the point originated over a rougher surface, it is reasonable to expect larger disturbances in the wind field and consequently, a larger roughness length.

### **3. Internal Boundary Layers over Heterogeneous Surfaces**

Often, the surface layer contains one or more *internal boundary layers* (IBLs) bounded above by a discontinuity in some variable or state of the surface layer (Garratt 1992). IBLs result from flow across surfaces that vary in any quantity capable of affecting the physical properties of the atmosphere (e.g., temperature, humidity, or surface roughness). Figure 2 is a schematic diagram that illustrates the concept of an IBL caused by a change in surface roughness.

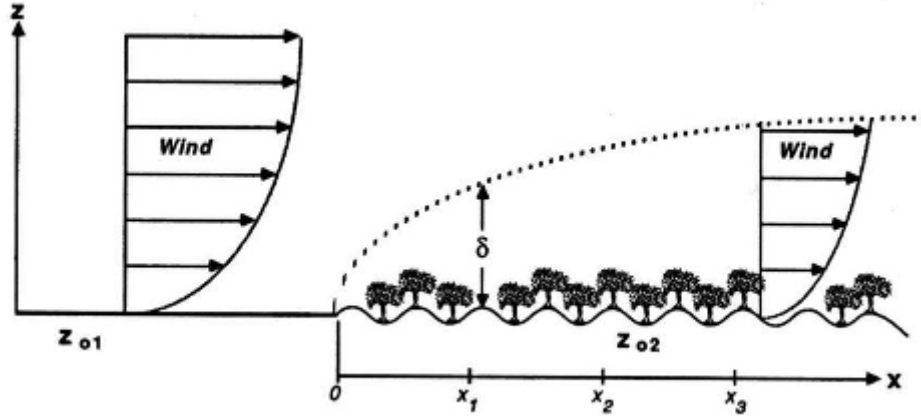


Figure 2. Diagram of an internal boundary layer. From Stull (1988).

Here, the height of the IBL,  $\delta$ , is a function of *fetch*, the distance downstream from the point roughness changes. In cases of significant heterogeneity, multiple IBLs may be present, each in response to an upstream surface. It is therefore important to recognize the presence of IBLs and interpret observations made over heterogeneous surfaces with care since Monin-Obukhov similarity fails in the transition region between an IBL and the advected boundary layer.

#### 4. Surface Flux Parameterization over Heterogeneous Surfaces

Early research in simulating surface fluxes in general circulation models (GCMs) mainly focused on parameterizing bulk exchanges of mass, momentum, and energy between homogeneous surfaces and the ABL. The resolution of early GCMs was on the order of tens to hundreds of kilometers, and necessarily dealt with surface roughness heterogeneities at the subgrid scale.

Louis (1979) devised a parameterization scheme for turbulent fluxes that included static stability effects and evaluated its performance in a 10-day forecast model. Due to its relative simplicity and brief calculation time, model developers incorporated this scheme, with occasional modifications, into many numerical models in the years following. Wang et al. (2002) proposed adaptations to

Louis's approach to better characterize fluxes over smooth surfaces and in cases where the effective roughness lengths for momentum and heat fluxes differ due to varying stability.

Beljaars and Holtslag (1991) considered the effects of variations in vegetative cover in aerial averaging techniques for parameterizing surface-layer fluxes. Their work showed a strong correlation between roughness length and surface heterogeneities located up to 5 km upwind of their observation site and suggested that wind gustiness could determine the effective local roughness length at such scales.

Two methods are commonly used to account for subgrid-scale surface heterogeneity in GCMs. The technique of *parameter aggregation* uses the fractional coverage of different surface types within a grid box to obtain grid-averaged parameters and then incorporates the subgrid averages into the bulk flux parameterization for the larger grid. The *flux aggregation* method uses bulk parameterization to obtain fluxes for each surface type and then determines grid-averaged fluxes based on the fractional coverage of each surface type within a grid box.

At higher resolution, aggregation of fluxes or parameters within a model grid box becomes less of a concern than the advection of these variables from neighboring grid boxes, particularly when surface heterogeneities are at least as large as the model resolution (personal communication, Wang 2010). This study is intended to address this issue by examining the variation of surface roughness with wind direction near a coastline.

### **C. PURPOSE AND OVERVIEW OF THESIS**

In this thesis, observational data from a dense network of meteorological sensors are examined to explore the relationships between roughness length in the lower atmosphere and physical properties of the surface. The purpose of this study is to demonstrate a local dependence of the downstream turbulent response to varying upstream surface features at different length scales and to

advocate the development of improved algorithms for incorporating this dependence in numerical weather and climate prediction models. The methodology includes analyzing time series and vertical profiles of measured and calculated variables in order to evaluate their spatial and temporal variations and to determine their relationships to surface roughness determined from satellite photographs.

This chapter included a brief introduction of terminology and concepts useful in this study. Chapter II presents essential concepts of thermodynamics of the lower atmosphere and introduces surface-layer similarity theory and flux-profile relationships. Chapter III describes the method of data collection and processing and the meteorological characteristics of the region for the cases presented. Chapter IV details the results and analyses from the selected cases, and Chapter V summarizes the results and concludes the thesis with a comparison of one of the chosen cases to numerical model output.

#### **D. MILITARY APPLICATIONS**

The modern military operates around the world in various terrains and land surface types, often in regions where weather observations are sparse. The development and implementation of high-resolution numerical models have aided the military weather community's mission to enhance operational safety while exploiting the weather for mission success. Communication via electromagnetic and electro-optical radiation, low-level aviation, and target acquisition and engagement, are all examples of military operations that are directly affected by weather conditions in the near-surface environment. Turbulence constantly alters the wind field, which influences the distribution of visibility restrictors such as low clouds, fog, haze, dust, and pollutants. An improved understanding of ABL structure, facilitated by studies such as this one, will lead to better techniques for simulating the effects of turbulent processes in numerical weather models that in turn lead to better forecasts.

## II. SURFACE-LAYER THERMODYNAMICS

### A. TURBULENT TRANSPORT

*Turbulence* describes a property of fluid flows characterized by strong spatial gradients in velocity. Turbulence in the ABL may be characterized by the presence of *eddies*, complete or semi-complete whorls of air that may be transported by the mean wind some distance downstream from their point of origin. These eddies scale on a spectrum of sizes ranging from a few millimeters to several hundred meters.

Boundary layer meteorologists typically classify turbulence according to the process that generated it. *Thermal turbulence* occurs when parcels of air become differentially buoyant by the addition or subtraction of thermal energy, most commonly from an underlying land surface heated by the Sun during the daytime or cooled at night. During the day, these parcels or “thermals” aggregate near the surface, forming eddies that rise semi-coherently to a height where their densities reach equilibrium with that of the surrounding air, at which point they lose upward momentum and may return to a lower level. The mean wind may also transport eddies responding to this thermally induced vertical motion some distance from their point of genesis. The resultant convective mixing of the ABL is a common daytime occurrence over land in temperate regions throughout the world. *Mechanical turbulence* in the ABL is associated with swirling air currents resulting from flow around surface features or along the interface of air masses with distinct densities. In general, shear increases (hence, turbulence is stronger) at higher wind speeds or when moving air contacts a rougher surface (Stull 1988).

Large eddies formed by either thermal or mechanical means generate smaller eddies inertially in high-shear regions near their edges, a process that effectively transfers *turbulence kinetic energy* (TKE) downscale. Taken together, these variously sized eddies comprise an energy spectrum for turbulence. TKE

contained in the largest eddies “cascades” through the inertial subrange, the domain of medium-sized (about  $10^2$  m) eddies. Just below the scale of the smallest eddies (about  $10^{-3}$  m), TKE is continually dissipated into heat by fluid viscosity. During this process, TKE is not a conserved atmospheric property; rather, conversion of TKE to internal energy is constantly occurring at the smallest turbulent scales (McWilliams 2006). Since the physical properties of the underlying surface greatly influence the production and evolution of both thermal and mechanical turbulence in the ABL, models attempting to approximate the complexities of turbulent transport near the Earth’s surface must incorporate accurate information about these properties.

## B. SURFACE-LAYER SCALING PARAMETERS AND FLUXES

A frequently used scaling parameter for turbulent processes in the surface layer is the *friction velocity*, denoted by  $u_*$ . This parameter represents the effects of surface wind stress and varies with both wind speed and surface roughness (Kaimal and Finnigan 1994). In general,  $u_*$  is given by

$$u_*^2 = \sqrt{\overline{u'w'^2} + \overline{v'w'^2}}. \quad (2)$$

(Here,  $u'$ ,  $v'$ , and  $w'$  are the horizontal and vertical components of air velocity due to turbulence.) For simplicity, ABL meteorologists typically orient their coordinate axes such that the abscissa corresponds to the direction the wind stress is applied (Stull 1988). In this case, one horizontal perturbation dimension is eliminated, and (2) reduces to

$$-u_*^2 = \overline{u'w'}, \quad (3)$$

Where, the negative sign is included to properly orient the sign of momentum transfer. Similarly, a scaling parameter for surface-layer virtual potential temperature (heat) and water vapor applications is introduced, defined by the following:

$$\theta_{v*} = -\frac{\overline{w'\theta'_v}}{u_*} \text{ and} \quad (4)$$

$$q_* = -\frac{\overline{w'q'}}{u_*}. \quad (5)$$

Possibly the most important diagnosis of the ABL that must be undertaken when characterizing turbulence potential is that of its *static stability*. Meteorologists usually classify a layer's static stability somewhat broadly as stable, unstable, or neutral. (Here, stability is qualified with the word "static" to imply that this atmospheric condition is independent of air motion.) At a specific location, if air with a particular density overlies less dense air (whether by contrasting temperature, humidity, or both), then the situation is unstable and the potential for spontaneous convective overturning exists. Instability in the boundary layer is usually a result of heating from below, although many processes tend to stabilize the boundary layer, including radiative emission and molecular diffusivity (Stewart 1979). Because air density (at constant pressure) is a function of temperature and water vapor content, absolute virtual potential temperature is used for calculations involving static stability in this study.

When quantifying stability, ABL meteorologists typically employ the concept of *flux*, which is the transport of a variable per unit area per unit time (Stull 1988). The transport of thermal energy, referred to hereon as heat, is used to demonstrate the concept of flux used by fluid dynamicists. The quantity  $\tilde{Q}_H$  is used to represent the transport of heat by a fluid medium through a particular area in a given time. Therefore, in SI units,  $\tilde{Q}_H$  is expressed in joules per square meter per second. However, atmospheric heat content is rarely measured in joules, so  $\tilde{Q}_H$  is converted to the more convenient *kinematic flux* form  $Q_H$  by dividing the flux by the product of the air density  $\rho_{air}$  and the specific heat of air at constant pressure  $C_p$ , yielding



$$Q_H = \frac{\tilde{Q}_H}{\rho_{air} C_p}. \quad (6)$$

Dimensional analysis of the result reveals the principal utility of this process; namely, that the quantity  $Q_H$  has dimensions of absolute temperature times velocity, both of which are routinely measured atmospheric fields. Moreover, except in extreme cases, the density of the lower atmosphere is roughly constant with height, typically varying by a factor of only 10% from the surface to the top of the ABL (Stull 1988). Using this assumption,  $\rho_{air}$  is taken to be constant rather than having dependence upon pressure and temperature, as in the equation of state for an ideal gas (Bohren and Albrecht 1998). To simplify calculations involving observed variables, ABL researchers routinely invoke similar reasoning in the literature; and hereinafter, use of the term *flux* implies kinematic flux.

### C. SURFACE-LAYER FLUX-PROFILE RELATIONSHIPS

Though our mathematical description of the physics is imperfect, many processes associated with turbulence in the ABL show remarkable regularity over a wide range of conditions in the field, suggesting the existence of functional relationships between the variables involved (Stull 1988). Historically, ABL meteorologists apply dimensional analysis techniques such as *Buckingham pi theory* to investigate these relationships. The concept of Buckingham pi theory is briefly introduced and its use is demonstrated by deriving expressions used in calculations for this study. For a thorough treatment of this and other similarity techniques, the reader is referred to Kaimal and Finnigan (1994).

In the surface layer, strong vertical (and horizontal) time-dependent gradients of momentum, mass, and energy often exist. However, the associated vertical fluxes of these quantities are nearly constant with height (Kaimal and Finnigan 1994). The objective of the procedure presented below is to determine

*flux-profile relationships*, empirical associations between the vertical gradients of these measured quantities and their vertical fluxes due to turbulent transport.

First, the process requires identifying variables of interest. In the case of turbulent transfer of momentum, the variables are:  $z$ , the local height above the surface;  $\frac{\partial \bar{u}}{\partial z}$ , the vertical gradient of the mean wind  $\bar{u}$ ;  $u_*$ , the friction velocity;  $\frac{g}{\theta_v}$ , a buoyancy parameter (to account for static stability); and  $\overline{w'\theta'_v}$ , the vertical turbulent heat flux. Since the units of these five variables comprise three fundamental dimensions—length, time, and absolute temperature—from pi theory, two nondimensional quantities  $\pi_1$  and  $\pi_2$  describe the transfer of momentum in the surface layer. Three of the five variables are selected as “key variables,” that together contain values expressed in all three relevant dimensions. The remaining two variables are expressed in terms of the key variables, raised to the unknown real exponents  $a - f$ , as follows:

$$\frac{g}{\theta_v} = u_*^a z^b (\overline{w'\theta'_v})^c \quad (7)$$

$$\frac{\partial \bar{u}}{\partial z} = u_*^d z^e (\overline{w'\theta'_v})^f. \quad (8)$$

Examination of the dimensions of the variables in these expressions leads to unique solutions for  $a - f$ , yielding the dimensionless quantities, or “groups,”

$$\pi_1 = z \frac{g}{\theta_v} \frac{\overline{w'\theta'_v}}{u_*^3} \text{ and} \quad (9)$$

$$\pi_2 = \frac{z}{u_*} \frac{\partial \bar{u}}{\partial z}. \quad (10)$$

To simplify the above groups, the Monin-Obukhov length  $L$  is introduced, defined by

$$L \equiv -\frac{u_*^3}{\kappa \frac{g}{\theta_v} \overline{w'\theta'_v}} \approx \frac{u_*^2}{\kappa \frac{g}{\theta_v} \theta_*}; \quad (11)$$

where the last expression invokes the approximation

$$\overline{w'\theta'_v} \approx -u_* \theta_*. \quad (12)$$

$\kappa$  is the dimensionless von Kármán constant, shown by analysis of field data to have a value between 0.35 and 0.43 (Stull 1988) (also included in the expression for  $\pi_2$ ). For calculations in this study, the most common approximation for the von Kármán constant is adopted,  $\kappa = 0.35$ .

Note that the sign of the Monin-Obukhov length is a stability indicator because it contains the turbulent heat flux term  $\overline{w'\theta'_v}$ , that undergoes a sign change when static stability changes. If in the surface layer  $\overline{w'\theta'_v} < 0$ , then  $L > 0$  and the heat flux is positive downward; hence, the layer is stable. Conversely, if  $\overline{w'\theta'_v} > 0$ , heat flux is positive upward,  $L < 0$ , and the layer is unstable. If there is no vertical turbulent heat flux (though turbulence can be present),  $\overline{w'\theta'_v} = 0$ ,  $L$  approaches (minus) infinity, and the layer is statically neutral.

From (9) and (11),  $\pi_1 = \frac{z}{L}$ . According to pi theory, there exists a functional dependence  $\phi$  (though not necessarily a unique one) between  $\pi_1$  and  $\pi_2$  expressed by the nondimensional gradient relationship

$$\pi_2 = \frac{\kappa z}{u_*} \frac{\partial \bar{u}}{\partial z} = \phi_m(\pi_1) = \phi_m\left(\frac{z}{L}\right), \quad (13)$$

with the subscript  $m$  used to indicate momentum. A similar procedure yields the gradient relationships for the mean virtual potential temperature profile

$$\phi_h\left(\frac{z}{L}\right) = \frac{\kappa z}{\theta_{v*}} \frac{\partial \bar{\theta}_v}{\partial z} \quad (14)$$

and the mean specific humidity profile

$$\phi_q\left(\frac{z}{L}\right) = \frac{\kappa z}{q_*} \frac{\partial \bar{q}}{\partial z}, \quad (15)$$

where  $\theta_{v*}$  and  $q_*$  are given by (4) and (5).

Pioneering research by Businger et al. (1971) and Dyer (1974) involving analysis of surface-layer observations over flat terrain in varying stability conditions yielded the following estimates for the momentum and heat flux-profile relationships  $\phi_m$  and  $\phi_{h,q}$ . (The flux-profile relationship for specific humidity and other scalar fields have the same functional form as that for heat.) These widely accepted empirical forms are used to analyze the data in this study:

$$\phi_m\left(\frac{z}{L}\right) = \begin{cases} \left[1 - \left(\frac{15z}{L}\right)\right]^{-1/4} & \text{for } \frac{z}{L} < 0 \text{ (unstable)} \\ 1 & \text{for } \frac{z}{L} = 0 \text{ (neutral)} \\ 1 + \left(\frac{4.7z}{L}\right) & \text{for } \frac{z}{L} > 0 \text{ (stable)} \end{cases} \quad (16)$$

$$\phi_{h,q}\left(\frac{z}{L}\right) = \begin{cases} 0.74 \left[1 - \left(\frac{9z}{L}\right)\right]^{-1/2} & \text{for } \frac{z}{L} < 0 \text{ (unstable)} \\ 0.74 & \text{for } \frac{z}{L} = 0 \text{ (neutral)} \\ 0.74 + \frac{4.7z}{L} & \text{for } \frac{z}{L} > 0 \text{ (stable)} \end{cases} \quad (17)$$

If measurements of the mean wind and absolute virtual potential temperature are available at two levels  $z_1$  and  $z_2$ , (13)–(15) are integrated using these limits to obtain

$$\bar{u}(z_2) - \bar{u}(z_1) = \frac{u_*}{\kappa} \int_{z_1}^{z_2} \phi_m \left( \frac{z}{L} \right) d \ln z \quad (18)$$

$$\bar{\theta}_v(z_2) - \bar{\theta}_v(z_1) = \frac{\theta_{v*}}{\kappa} \int_{z_1}^{z_2} \phi_h \left( \frac{z}{L} \right) d \ln z \quad (19)$$

$$\bar{q}(z_2) - \bar{q}(z_1) = \frac{q_*}{\kappa} \int_{z_1}^{z_2} \phi_q \left( \frac{z}{L} \right) d \ln z. \quad (20)$$

or

$$u_* = \frac{\kappa [\bar{u}(z_2) - \bar{u}(z_1)]}{\int_{z_1}^{z_2} \phi_m \left( \frac{z}{L} \right) d \ln z} \quad (21)$$

$$\theta_{v*} = \frac{\kappa [\bar{\theta}_v(z_2) - \bar{\theta}_v(z_1)]}{\int_{z_1}^{z_2} \phi_h \left( \frac{z}{L} \right) d \ln z} \quad (22)$$

$$q_* = \frac{\kappa [\bar{q}(z_2) - \bar{q}(z_1)]}{\int_{z_1}^{z_2} \phi_q \left( \frac{z}{L} \right) d \ln z}. \quad (23)$$

Although the integrals in (21) – (23) are expressible in closed form, they must be solved iteratively to obtain  $u_*$ ,  $\theta_{v*}$ , or  $q_*$ , since the integrand includes  $L$  that involves these unknowns. For calculations involving (20) – (22) undertaken in this study, for a reasonable initial approximation of  $u_*$ ,  $\theta_{v*}$ , or  $q_*$ , 100 iterations converged at far greater precision than the data used in the calculation.

If measurements of the mean wind and virtual potential temperature are available at only one level  $z$ , (21) – (23) are supplemented with properties from the roughness height  $z_0$ ; namely, over open ocean the Charnock relation (1) and the assumptions that  $\bar{\theta}_{sea} = \bar{\theta}(z_0)$ ,  $q_s(\theta_{sea}) = \bar{q}(z_0)$  and in general, that  $\bar{u}(z_0) = 0$ .

With these substitutions, the integrals in (21) – (23) are then evaluated from  $z_0$  to  $z$  to obtain an expression for the mean wind as a function of height, from which  $z_0$  can be determined.

#### D. BULK AERODYNAMIC PARAMETERIZATIONS

In practice, most numerical models incorporate the effects of surface roughness by parameterizations based on the bulk aerodynamic formulae. The following is a brief introduction of the concept, adapted from Wang (2009).

The *drag coefficient*  $C_z$  at height  $z$  is defined as follows:

$$C_z \equiv \left( \frac{u_*}{\bar{U}_z} \right)^2, \quad (24)$$

where  $\bar{U}_z$  is the mean wind at height  $z$ . Researchers working within the surface layer generally adopt a standard reference height (or the height at which they measure the wind). At the World Meteorological Organization's (WMO) standard 10-m height for wind observations,  $C_z$  is designated  $C_D$ . In (24), this becomes

$$C_D = \left( \frac{u_*}{\bar{U}_{10}} \right)^2. \quad (25)$$

Substituting Equation (3), the turbulent momentum flux is given by

$$\overline{u'w'} = -C_D \bar{U}_{10}^2 = -u_*^2 \quad (26)$$

and using Equation (21),  $C_D$  is given by

$$C_D = \left( \frac{\kappa}{\int_{z_0}^{10} \phi_m \left( \frac{z}{L} \right) d \ln z} \right)^2. \quad (27)$$

Similarly, the heat exchange coefficient  $C_H$  (at 10 m) is given by

$$C_H^2 = C_D \left( \frac{\theta_{v^*}}{\bar{\theta}_{10} - \bar{\theta}_{z_0}} \right)^2 = C_D \left( \frac{\kappa}{\int_{z_0}^{10} \phi_h \left( \frac{z}{L} \right) d \ln z} \right)^2. \quad (28)$$

### **III. OBSERVATIONS AND SELECTED CASES**

#### **A. SURFACE-LAYER OBSERVATIONS**

The National Aeronautics and Space Administration (NASA) Headquarters Weather Support Office and Cape Canaveral Air Force Station (CCAFS) jointly operate the Weather Information Network Display System (WINDS), part of an extensive meteorological observation program on and in the region surrounding CCAFS and the Kennedy Space Center (KSC) in Florida. In continuous operation since 1986, the WINDS collects, archives, and disseminates observations measured by a suite of over 200 wind, temperature, humidity, and pressure sensors attached to 46 instrumented towers distributed across a 1,200-km<sup>2</sup> region (Figure 3). The primary objective of the WINDS is to provide 45th Weather Squadron, NASA Safety, and Range Safety personnel with a comprehensive, real-time description of weather conditions from the surface to 150 m in support of the KSC spaceflight mission (Computer Sciences Raytheon [CSR] 2006). This study utilizes observations recorded at 5-minute intervals from selected WINDS towers.





Figure 3. WINDS tower distribution on and near CCAFS on the Atlantic Coast of Florida. After CSR (2006).

WINDS towers at CCAFS are classified into three categories based on their primary operational function: launch critical, safety critical, and forecast critical towers. The four-digit tower identification number is decoded (except for Towers 9001 and 9404) as follows: the first pair of digits is the tower's distance from the outer coastline, and the second pair of digits is its latitudinal distance from Port Canaveral (red star in Figure 3). Both coded distances are rounded to the nearest integer in nautical miles. The Appendix contains tables of tower locations and instrumentation heights by tower type.

### 1. Launch Critical Towers

The four launch critical towers are located nearest the active launch complexes and the Space Shuttle Landing Facility. Since mission planners use observations from launch critical towers to directly evaluate launch safety criteria, their accuracy and reliability requirements are the highest in the WINDS. Towers 0002, 0006, 0110, and 0313 all contain redundant instrumentation at multiple

levels and are equipped with battery backup to ensure data availability for up to 24 hours following a power failure. Horizontal supports for wind equipment and temperature sensors are aligned northwest to southeast on Towers 0002, 0006, and 0110 and northeast to southwest on Tower 0313 (Figure 4).



Figure 4. Photograph of the upper levels of Tower 0313, a 150-m launch critical mast. Note the dual instrumentation on horizontal supports at each level. From CSR (2006).

## **2. Safety Critical Towers**

Fourteen safety critical towers are primarily located near facilities where toxic materials such as vehicle propellants are stored (CSR 2006). Safety critical towers support wind equipment at 3.7 m and 16.5 m and temperature sensors at 1.8 m and 16.5 m. Since relative humidity is not measured at these locations, the potential temperature  $\theta$  is used in calculations involving observations from safety critical towers instead of virtual potential temperature  $\theta_v$ . Figure 5 is a photograph of a typical safety critical tower.



Figure 5. Photograph of a typical safety critical tower. From CSR (2006).

### **3. Forecast Critical Towers**

Nineteen forecast critical towers are primarily distributed in the region surrounding CCAFS (Figure 3). Observations from these towers are used for general weather support and resource protection functions. Like launch critical and safety critical towers, forecast critical towers house temperature sensors at 1.8 m, but they report wind data from one level only (16.5 m) (CSR 2006). Because forecast critical towers lack multilevel observations of wind and temperature, observations recorded at these locations were not used in this study.

### **4. Data Processing**

For this study, observations were provided with the following precisions: air temperature and dew point, 0.1 °F; surface pressure (Tower 0313 only), 0.1 hPa; wind speed, 1 knot; and wind direction, 1°. Prior to using these observations to derive roughness length, friction velocity, and heat fluxes, the

data were converted to corresponding SI units and subjected to quality control algorithms that excluded missing and unphysical values. Additionally, since the observation interval is 5 minutes, all variables were averaged over 20 minutes in order to more accurately represent mean conditions. Due to the relatively coarse precision of wind speed measurements, observations taken when speed differences between the two levels did not exceed 1 knot (about  $0.5 \text{ ms}^{-1}$ ) were excluded from calculations of  $z_0$ ,  $u_*$ , and heat fluxes.

Figures 6 and 7 are time series of observed conditions and calculated quantities for the northeast sensors at the lowest levels (referred to in this study as levels 1 and 2) of Tower 0313 on 2–5 May 2008. Horizontal axes for all time series presented herein are labeled with the day of the year. Local midnight corresponds to the day number tick mark, and local noon coincides with an unlabeled tick mark. Regardless of the date, time is given in Eastern Standard Time (EST) without correcting for Daylight Savings Time.

In Figures 6a and 6b, virtual potential temperature ( $\theta_v$ ) and specific humidity ( $q$ ) are shown for the 1.8-m (red) and 16.5-m (blue) sensors. Figures 6c and 6d contain time series of the calculated sensible heat flux (SHF) and latent heat flux (LHF). For the flux plots, thermally unstable (red) and stable (blue) conditions are determined by the  $\theta_v$  difference between the indicated levels. Diurnally-cycling stability fluctuations and low-level moisture redistribution are evident in the  $\theta_v$  and  $q$  trends, and both phenomena appear reasonable in magnitude and duration. Similarly, fluxes during peak afternoon heating fall within normal ranges for the latitude and season (personal communication, Wang 2010).

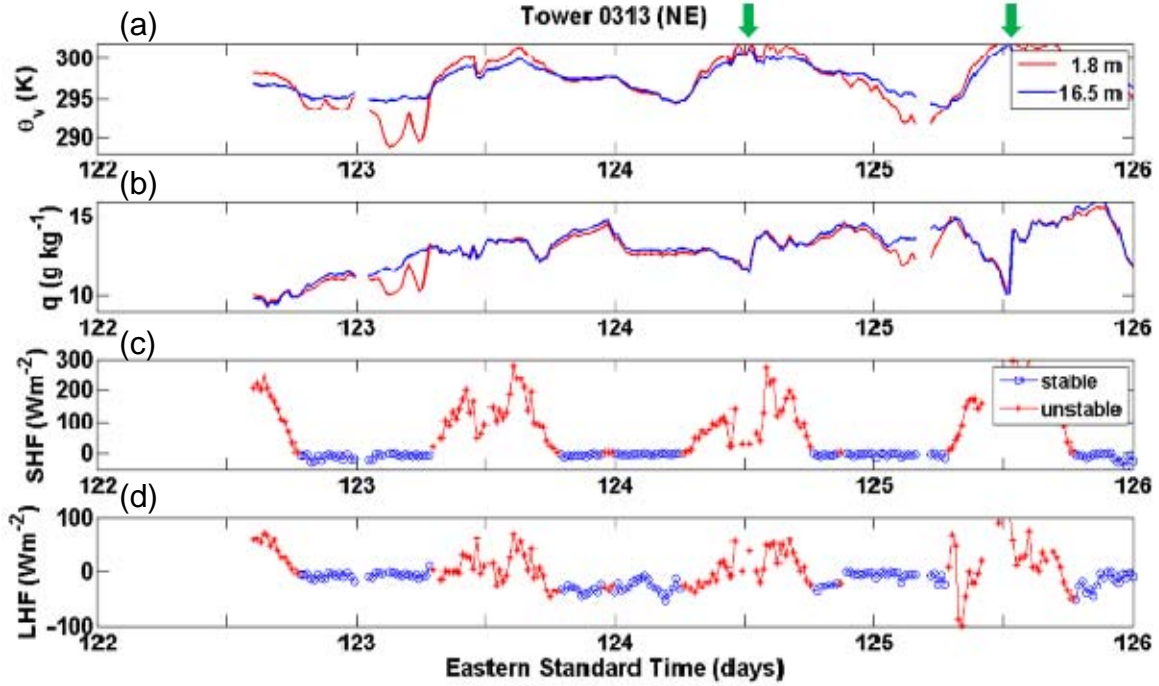


Figure 6. Temporal variation of observed (a) absolute virtual potential temperature ( $\theta_v$ ) and (b) specific humidity ( $q$ ) in g kg<sup>-1</sup> and calculated (c) sensible and (d) latent heat fluxes in Wm<sup>-2</sup> from the northeast sensors at temperature levels 1 and 2 of Tower 0313 on 2–5 May 2008.

Figures 7a and 7b contain the wind speed (WS) and wind direction (WD) observations for the 3.7-m (red) and 16.5-m (blue) sensors. (Note that the height of the lowest wind observation differs from that of temperature and humidity [cf. Appendix]. The designation "level 1" is used herein to refer to both the lowest levels for wind and temperature. Context clarifies whether "level 1" refers to the lowest level of wind or temperature measurement.) On days 122–124, progression of the synoptic-scale pattern induced a gradual veering from southeasterly to southwesterly flow, with higher wind speeds observed during the daylight hours than at night. Figures 7c and 7d are the roughness length ( $z_0$ ) and friction velocity ( $u_*$ ) calculated from observations at the indicated levels and shown in red or blue based on the same convention for stability as in Figures 6c and 6d.

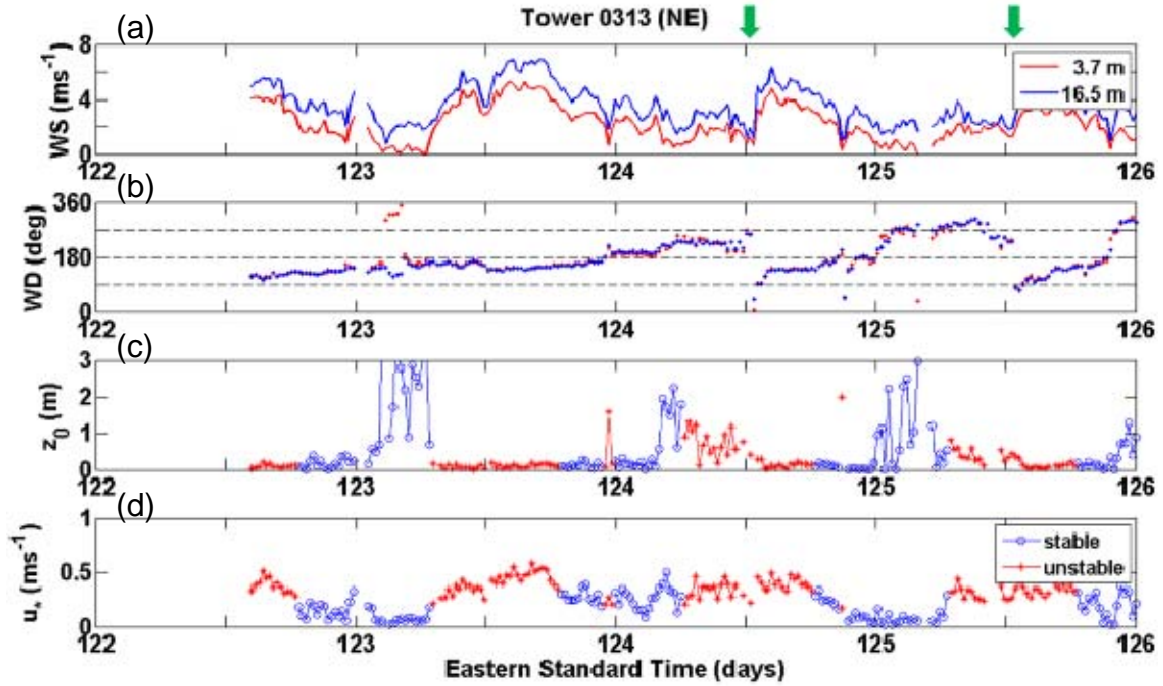


Figure 7. Temporal variation of observed (a) wind speed (WS) in  $\text{ms}^{-1}$  and (b) wind direction (WD) in degrees and calculated (c) roughness length ( $z_0$ ) in m and (d) friction velocity ( $u_*$ ) in  $\text{ms}^{-1}$  from the northeast sensors at wind levels 1 and 2 of Tower 0313 on 2–5 May 2008.

During most of this four-day period,  $z_0 \leq 0.5$  m, and  $u_*$  ranges between 0.2 and 0.6  $\text{ms}^{-1}$ . However, between midnight and sunrise of day 123 and for most of the first half of day 124, unreasonably large  $z_0$  values are calculated. During both of these periods, relatively low wind speeds ( $< 2 \text{ ms}^{-1}$ ) are observed. In addition, large temporal variations in  $z_0$  are noted during these periods. Similar trends in roughness length are observed throughout the year during periods of low wind speeds, often occurring overnight. Calculated roughness lengths during these periods are considered unphysical for two reasons. First, the wind speed precision (0.5  $\text{ms}^{-1}$ ) is a relatively high percentage of the wind speed. The second reason is that Monin-Obukhov similarity theory is not applicable in low wind speed conditions, especially for nocturnal stable boundary layers in which

turbulence is weak and intermittent. For this reason, in the remainder of the time series shown herein, results for  $z_0$  are not plotted if the wind speed at either level is less than  $2 \text{ ms}^{-1}$ .

Gaps in the time series of measured fields (seen before noon on day 122 and near midnight on day 123) correspond to periods for which no measurement is available, although this does not usually indicate a sensor has failed. Rather, the problem appears to occur in either the data acquisition or storage system for the particular level or tower, since these gaps usually occur simultaneously for both wind and temperature sensors, often at multiple levels. Gaps in the derived quantities signify at least one of the following conditions: (1) lack of one or more measurements required for the calculation, (2) failure to exceed the  $0.5 \text{ ms}^{-1}$  speed shear criterion between the indicated levels, (3) wind speed at either level is below  $2 \text{ ms}^{-1}$ , or (4) wind speed at the lower level exceeds that of the higher level.

## **B. CASES SELECTED FOR THIS STUDY**

### **1. Surface Morphology**

Located on the East Coast of the Florida Peninsula, the region surrounding CCAFS contains diverse types of surfaces including urban areas, marshes, temperate forests, barrier islands, sheltered inland waters, and the Atlantic Ocean. Depending upon the strength and direction of the surface-layer wind field, turbulent eddies generated by flow over these heterogeneous surfaces vary in dimension and impart varying gustiness downstream.

The most conspicuous disparity in surface roughness at CCAFS exists between land and ocean. In order to investigate the turbulent response that arises from this heterogeneity, periods are identified during which near-surface winds originated over land (westerly) and ocean (easterly). These opposite flow regimes should be selected closely in time to minimize the effect of variations in atmospheric stability, cloud and precipitation forcing, and foliation. Within this framework, this study focused on examining the turbulent response at WINDS

towers near the coast during a diurnally cycling coastal wind circulation event in June 2008 and the passage of Tropical Storm Fay in August 2008. Wind direction changes of about 180° occur within 10–20 minutes in the coastal wind cases and in less than 12 hours during the tropical storm.

## **2. Coastal Wind Circulations**

Occurring at any time of the year, but most prevalent from late spring throughout the warm season, differential heating of land and water surfaces near CCAFS gives rise to diurnally cycling coastal winds, commonly referred to as *sea breezes* during the daytime and *land breezes* at night. The leading edge of the sea breeze defines a mesoscale thermodynamic discontinuity called the *sea-breeze front* (SBF), the passage of which is usually accompanied by a slight decrease in temperature and a sharp increase in humidity. During periods of relatively weak synoptic forcing, the afternoon SBF may travel several tens of kilometers inland and trigger numerous showers and thunderstorms over the Peninsula.

Numerous studies of coastal wind circulations at Cape Canaveral have been conducted *in situ* using Doppler radar and cloud photogrammetry (Wakimoto and Atkins 1993); observations (Reed 1979); aircraft soundings (Laird et al. 1995); and with high-resolution mesoscale modeling (Rao and Fuelberg 2000), (Manobianco et al. 1996), and (Baker et al. 2000). In particular, Reed (1979) demonstrated from observations at Tower 0313 that a discernible diurnal oscillation between onshore and offshore wind components was present year-round, with the largest amplitude occurring in May and the smallest in January. Reed also found the largest amplitudes were observed by the highest anemometer (then 151 m) and that with few exceptions, the sea/land-breeze circulation shifted clockwise (veered) with time, roughly completing a circuit of the compass in one day.



In Figures 6 and 7, green arrows indicate the passage of two SBFs around noon on days 124 and 125 (4–5 May 2008). SBF passage is most readily indicated (in this region) by the sudden backing of the wind direction from southwest to southeast and the rapid increase in  $q$ . In addition, wind speeds at the 16.5-m sensor increase from about  $2 \text{ ms}^{-1}$  to  $6 \text{ ms}^{-1}$ , and temperatures at both levels gradually fall following SBF passage. The response of roughness length to coastal wind circulations is discussed in Chapter IV.

Figure 8 contains vertical profiles of  $\theta_v$ ,  $q$ , wind speed, and wind direction observed from the northeast sensors of Tower 0313 at 4-hour intervals beginning at 0500 EST on 4 May 2008. Such plots are useful for evaluating the evolution and vertical variation of these measured fields. As with time series presented in this study, observed quantities in vertical profiles are averaged over a 20-minute window centered on the indicated time. In Figure 8a, at 0500 EST (about 1 hour prior to sunrise), the surface layer is thermally stable. With daytime heating, the lowest layers become increasingly unstable. Around 1300 EST, a SBF passed the tower location. In Figures 8c and 8d, the wind profiles at 1300 EST indicate that the SBF had passed the sensors at wind levels 1–4, but had not yet passed the higher levels of the tower. The uniform directional profile shown before and after SBF passage was typically observed on days affected by these coastal wind circulations. In Figure 8c, logarithmic wind profiles that fit to observations from the lowest two levels are plotted on the wind speed profiles in blue dashed lines. These idealized profiles are constructed for the neutral stability condition using the methodology presented in Chapter II.

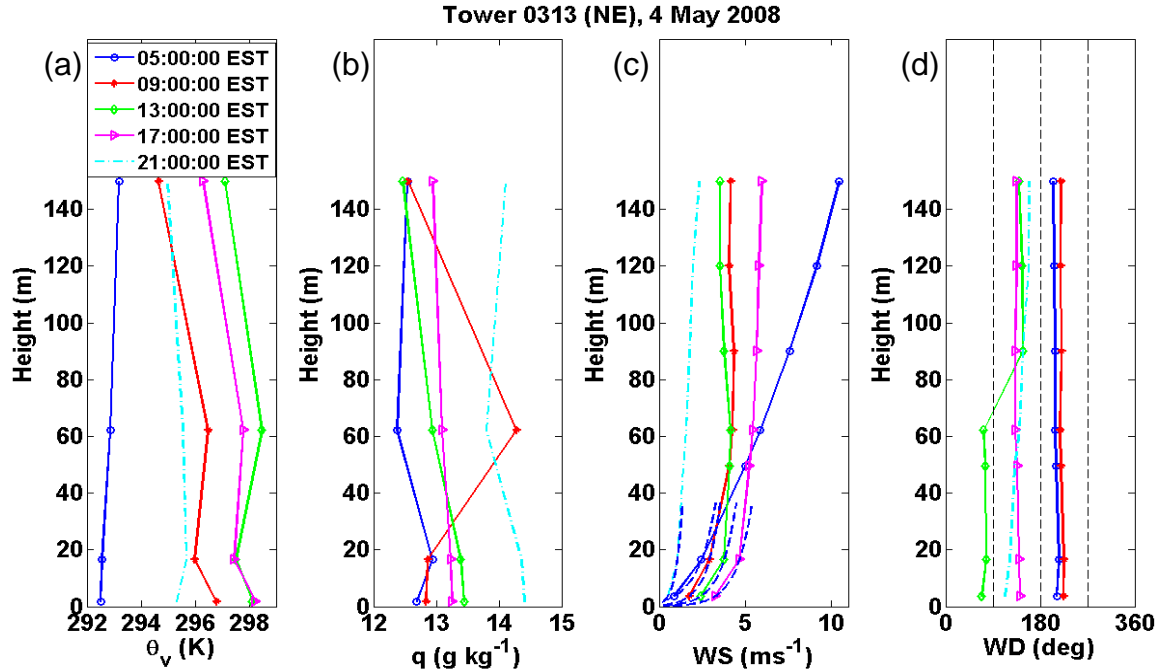


Figure 8. Vertical variation of observed (a) virtual potential temperature ( $\theta_v$ ), (b) specific humidity ( $q$ ), (c) wind speed (WS), and (d) wind direction (WD) from the northeast sensors of Tower 0313 on 4 May 2008.

### 3. Tropical Storm Fay

The easterly wave that spawned Tropical Storm Fay moved off the coast of Africa on 6 August 2008 and rapidly crossed the Atlantic Ocean before slowing and becoming better organized over the Greater Antilles. On 15 August, Fay was upgraded to tropical storm status while over land on the island of Hispaniola. Under favorable upper-level wind conditions and despite interacting with mountainous terrain, Fay continued to strengthen slowly and made two landfalls in Cuba before turning northward toward the Florida Keys (Stewart and Beven 2009). On 19–21 August, Tropical Storm Fay crossed the central Florida Peninsula before making its third Florida landfall near Flagler Beach about 120 km north of CCAFS (Figure 9). While near CCAFS, the system's forward speed slowed to 3–4 knots, resulting in 16.5-m sustained winds averaging above  $8 \text{ ms}^{-1}$  for 48 hours at most WINDS locations.

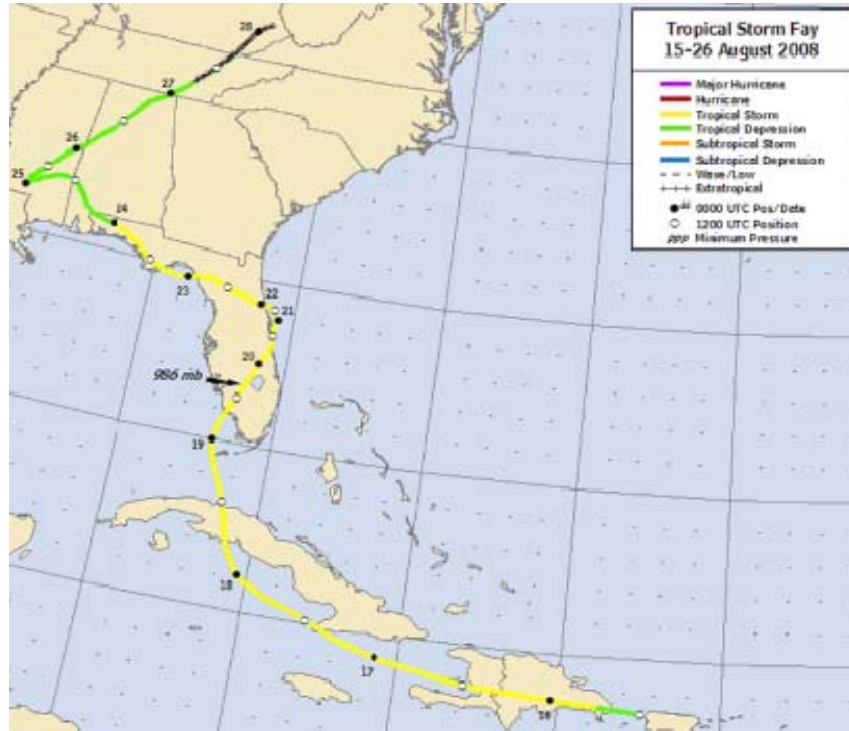


Figure 9. Track of the center of Tropical Storm Fay. From Stewart and Beven (2009).

Tropical Storm Fay proved to be an ideal case for this study for several reasons. First, the track of Fay caused winds to shift within 12 hours from a strong onshore to a strong offshore component. Also, Fay's prolonged residence time near CCAFS resulted in longer-fetch surface-layer winds than would be induced by smaller-scale flow regimes. Additionally, fewer wind observations were excluded from calculations during Fay due to the minimum speed shear criterion of  $0.5 \text{ ms}^{-1}$ . This is a result of both the relatively low ratio of this threshold to higher wind speeds and to the tendency of stronger wind profiles to exhibit significant shear in the surface layer over land. In such strong wind profiles, generation of ABL turbulence by low-level wind shear dominates thermal turbulence production, and surface-layer stability becomes almost thermally neutral. Consequently, uncertainties associated with quantities dependent on thermal stability, such as those in the Monin-Obukhov similarity functions (16) and (17), are minimized.

Figure 10 shows time series of observed conditions and calculated variables from the southeast sensors of Tower 0006 during the passage of Tropical Storm Fay on 18–21 August 2008. Variation in all quantities decreases on days 232–233 due to clouds and precipitation associated with the tropical storm.

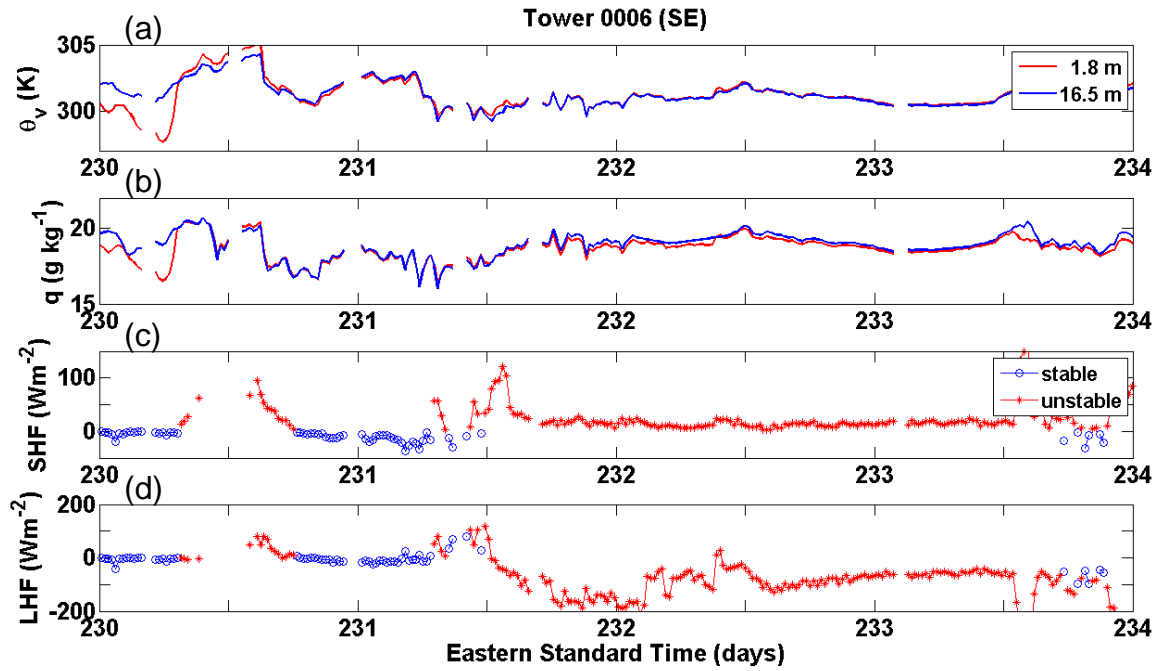


Figure 10. Same as Figure 6, except observed conditions and calculated quantities are from the southeast sensors at temperature levels 1 and 2 of Tower 0006 on 18–21 August 2008.

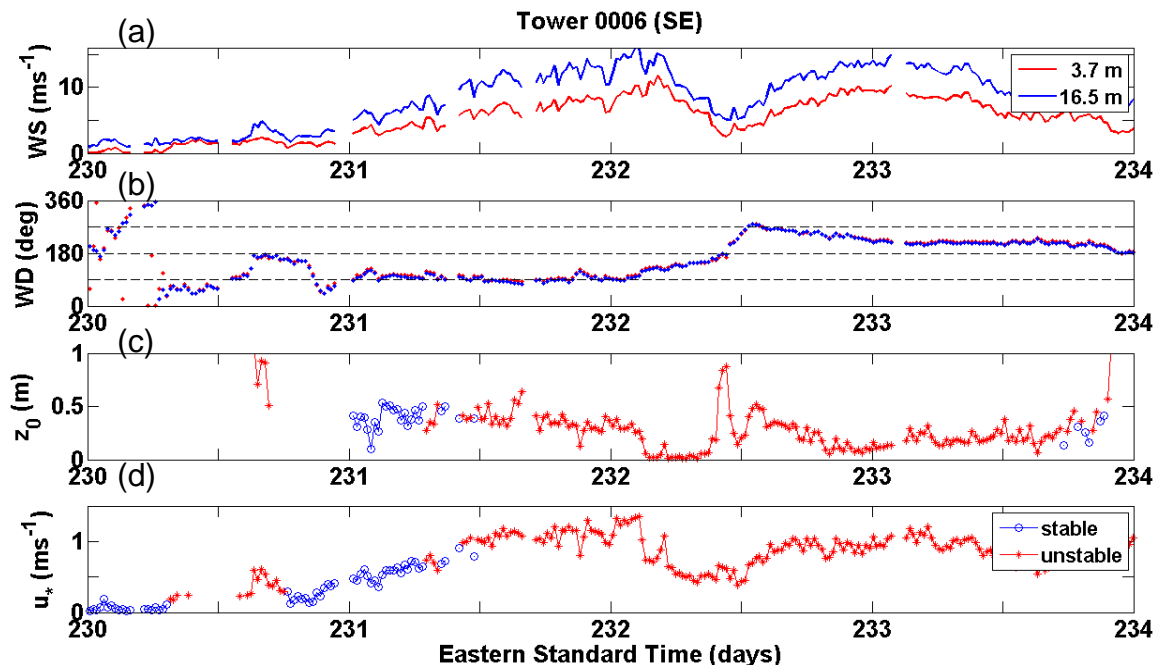


Figure 11. Same as Figure 7, except observed conditions and calculated quantities are from the southeast sensors at wind levels 1 and 2 of Tower 0006 on 18–21 August 2008.

Figures 11a and 11b contain time series of the wind speed and direction observed at Tower 0006 during Tropical Storm Fay. While the center of Fay was located south of CCAFS over the Florida Peninsula on days 230 and 231, flow was generally from the east. As Fay approached Cape Canaveral, wind speeds increased, reaching a maximum of about  $16 \text{ ms}^{-1}$  at 16.5 m on day 232. The decrease in wind speed during the morning hours of day 232 occurred while the center of Fay was near CCAFS (cf. Figure 9). During about a 12-hour period, the wind direction veered to the west and speeds increased as Fay moved north of CCAFS. The response of roughness length during Tropical Storm Fay is discussed in Chapter IV.

Figure 12 contains vertical profiles of observed conditions recorded by the southeast sensors of Tower 0006 at 4-hour intervals beginning at 0400 EST on 20 August 2008. In Figure 12a, the near-neutral thermal stability condition is evidenced by the nearly vertical  $\theta_v$  profiles. Figures 12c and 12d depict the wind

profiles before and after the center of Fay crossed the latitude of the tower, with southeasterly flow at 0400 EST and 0800 EST and southwesterly flow thereafter.

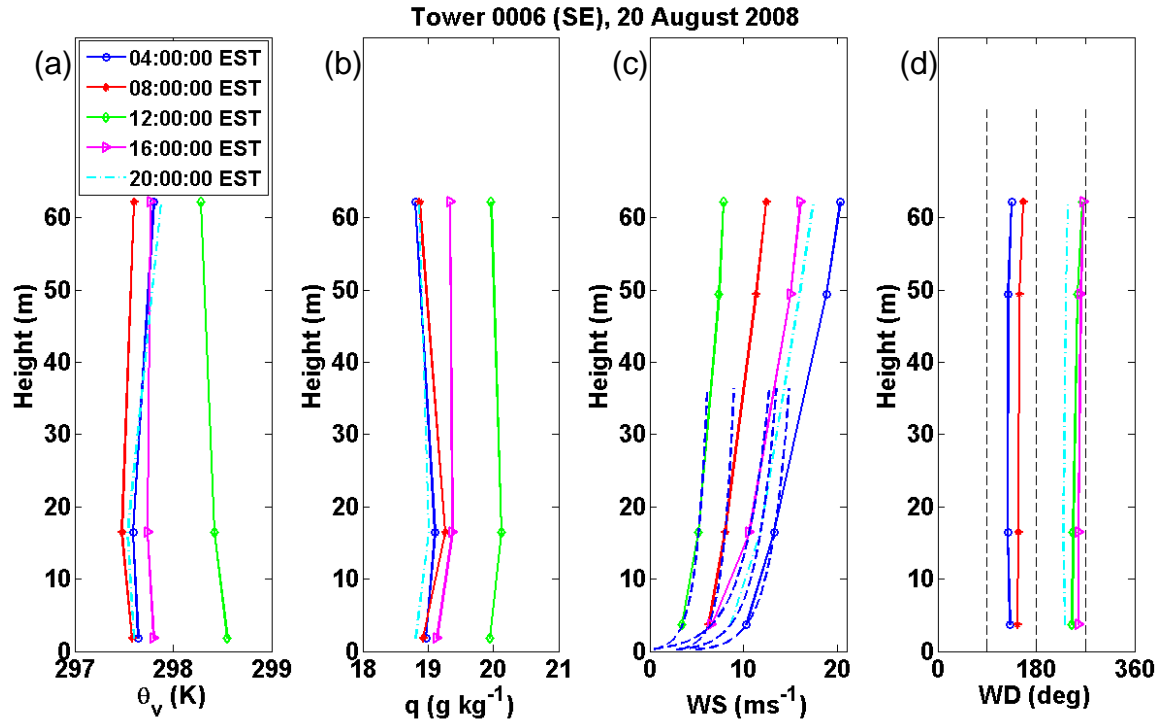


Figure 12. Same as Figure 8, except observed conditions are from the southeast sensors of Tower 0006 on 20 August 2008.

THIS PAGE INTENTIONALLY LEFT BLANK

## **IV. RESULTS AND ANALYSES**

### **A. ROUGHNESS LENGTH VARIATION IN RESPONSE TO COASTAL WIND CIRCULATIONS**

On 1–4 June 2008, a series of coastal wind circulations occurred at CCAFS, and these were recorded at WINDS locations near the coast. Daily mesoscale sea breezes are a common occurrence in the region throughout the warm season, but this period was particularly selected for its lack of significant convective activity in the vicinity of CCAFS. Although Monin-Obukhov surface-layer similarity can be applied to convective winds, precipitation-induced outflows often disrupt the repetitive signals in observations of the diurnal coastal wind cycle, and it is this regularity this study sought to investigate.

#### **1. Tower 0006**

Tower 0006 is a launch critical tower located approximately 600 m from the shoreline (Figures 3 and 13). At higher magnification (Figure 14), the landscape within a 200-m radius of Tower 0006 consists of mainly shrubs and small trees, the largest of which (using a qualitative shadow analysis technique) lie in sectors  $040^{\circ}$ – $120^{\circ}$ ,  $150^{\circ}$ – $190^{\circ}$ , and  $330^{\circ}$ – $350^{\circ}$ . (Herein, all sectors and radials are presented with reference to the tower and are estimated to the nearest  $10^{\circ}$  using satellite imagery.) Within a 50-m radius of Tower 0006, an "X"-shaped area of cleared ground contains the attachments for the tower's guy wires. Variations of this clearing are present at each launch critical tower.





100 m

Figure 13. Satellite photograph of Tower 0006 and surrounding area. Red "X" marks the tower location. In all satellite photographs presented herein, true north, or 360°, is oriented toward the top of the image. Image ©2010 Google.



50 m

Figure 14. Satellite photograph of Tower 0006 and immediate surroundings. Red "X" marks the tower location. Image ©2010 Google.

Figures 15 and 16 are time series showing observations and calculated quantities from the southeast sensors at levels 1 and 2 of Tower 0006 on 1–4 June 2008. In Figure 15a, the diurnal temperature variation is observed at both levels. The magnitude of the temperature change is greater for the lower level. In Figure 15b, specific humidity decreases due to vertical mixing during the morning hours then rises rapidly in the marine air following each SBF. In Figures 15c and 15d, diurnal variation in surface-layer thermal stability and in the calculated SHF and LHF values are also apparent. Maximum values for SHF and LHF during the daytime reach about 300 and 200  $\text{Wm}^{-2}$ , respectively.

In Figures 16a and 16b, wind speed and direction indicate the passage of four SBFs before noon each day (indicated throughout by green arrows). Following each SBF, wind speeds increase and the flow backs rapidly from the southwest to the southeast, followed by a gradual veering to the southwest during the remainder of the day and overnight. Maximum wind speeds of about  $5 \text{ ms}^{-1}$  at both levels occur following the SBF each afternoon, and the weakest winds are observed around midnight. The calculated friction velocity  $u_*$ , shown in Figure 16d, ranges between 0.1 and  $0.5 \text{ ms}^{-1}$ , a typical range for surface layers over land at these wind speeds. Figure 16c contains the calculated roughness length  $z_0$ , which is mostly less than 0.25 m. As stated in Chapter III, no  $z_0$  value is plotted when the wind speed at either level is less than  $2 \text{ ms}^{-1}$ .

On all four days, the lowest  $z_0$  values for levels 1 and 2 were recorded when the wind direction was from sector  $120^\circ$ – $150^\circ$ , which is seen in Figure 14 to roughly correspond to an opening in the trees connecting ground in the immediate vicinity of Tower 0006 to close-cut grass and roads near buildings located 200 m southeast of the tower. At approximately this distance in any other direction from the tower, more numerous low shrubs and trees are present, and when the flow is from these sectors, higher  $z_0$  values are calculated for levels 1 and 2.

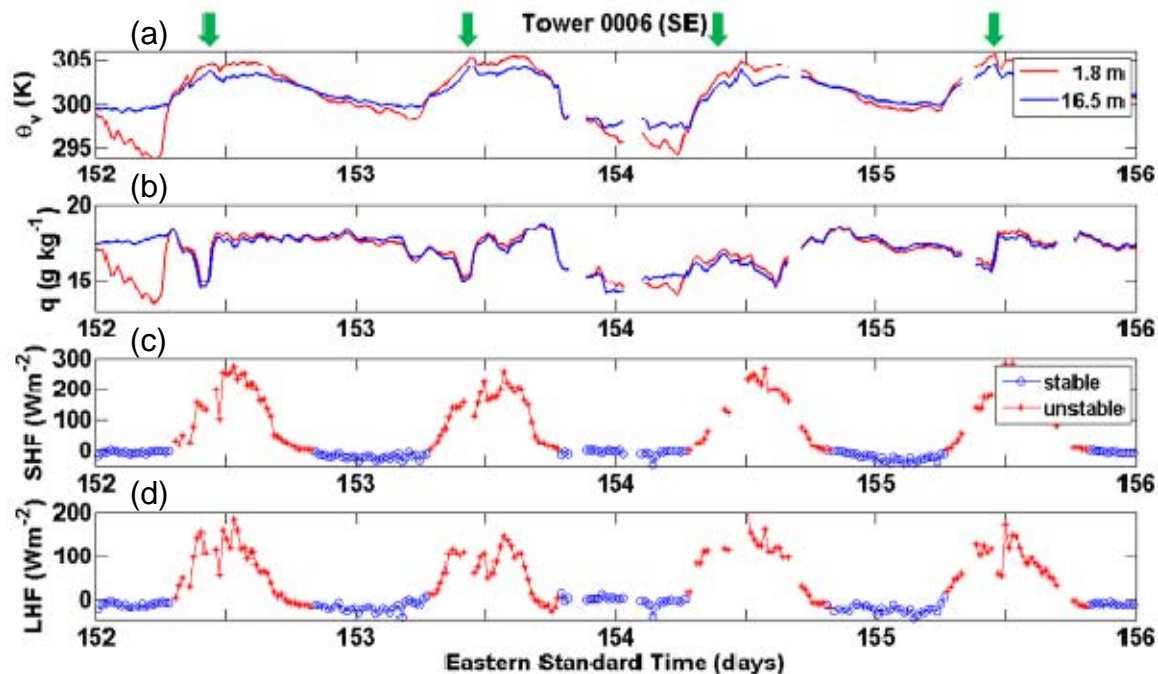


Figure 15. Same as Figure 6, except observed conditions and calculated quantities are from the southeast sensors at temperature levels 1 and 2 of Tower 0006 on 1–4 June 2008.

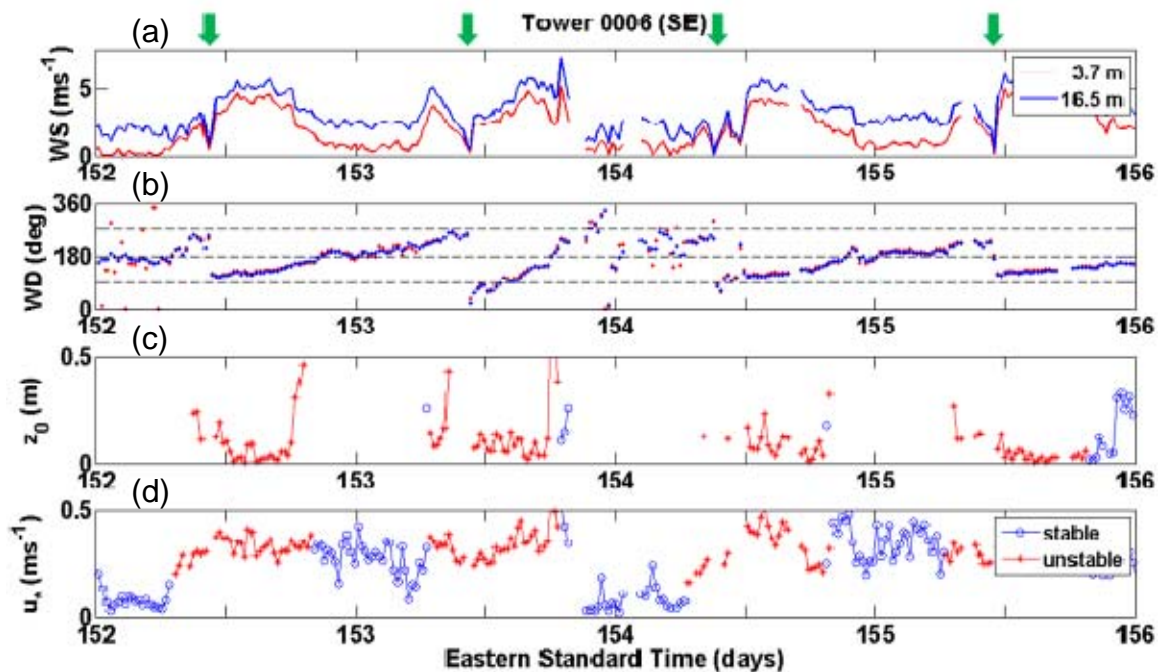


Figure 16. Same as Figure 7, except observed conditions and calculated quantities are from the southeast sensors at wind levels 1 and 2 of Tower 0006 on 1–4 June 2008.



Figure 17 is similar to Figure 16, except quantities are from wind levels 2 and 3 of Tower 0006. Since temperature and humidity measurements are not recorded at wind level 3, those from levels 1 and 2 (Figure 15) are used to obtain  $z_0$  and  $u_*$  at levels 2 and 3. Also, due to the lack of temperature sensors at level 3, heat fluxes calculated using wind levels 2 and 3 and temperature levels 1 and 2 are very similar to those in Figures 13c and 13d and are not shown for this case. Although wind speed at level 3 also decreases overnight, winds are generally stronger at this level, most notably following each SBF.

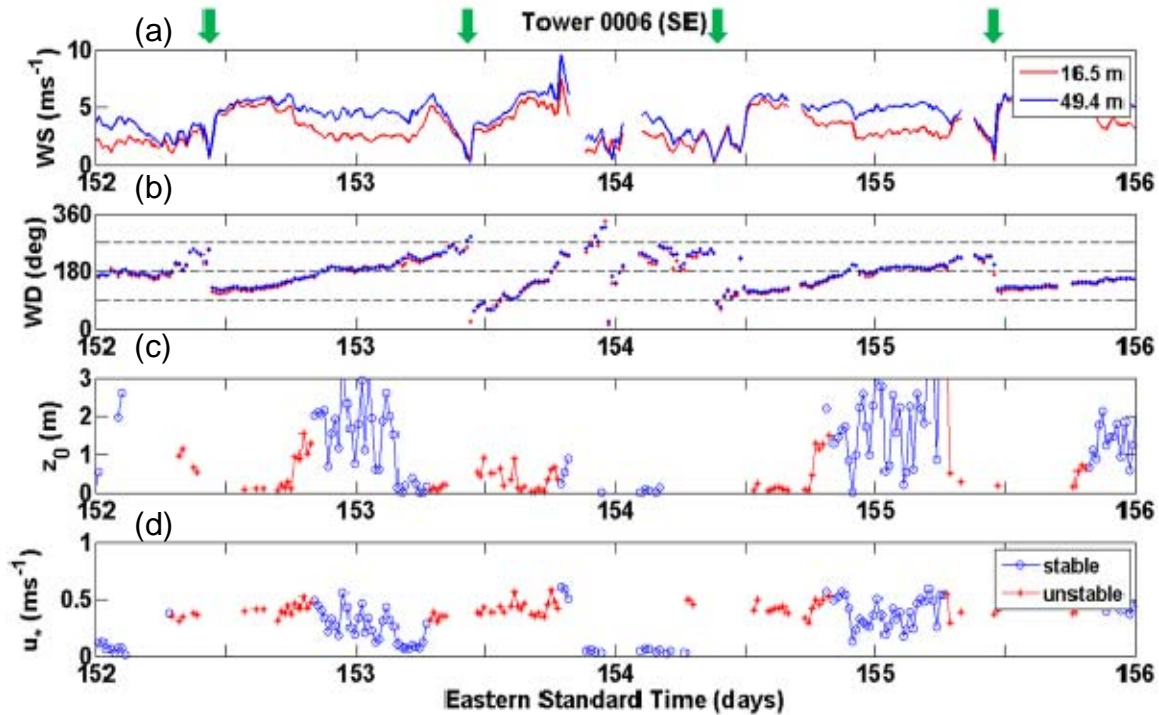


Figure 17. Same as Figure 7, except observed conditions and calculated quantities are from the southeast sensors at wind levels 2 and 3 of Tower 0006 on 1–4 June 2008.

Consistent with results from wind levels 1 and 2, at wind levels 2 and 3 the lowest  $z_0$  values occur when the wind direction is from sector  $120^\circ$ – $140^\circ$  on days 152–154. Again, this response appears to be related to the smoother landscape in this sector (cf. Figure 13), though the distance to the surface inducing the low

$z_0$  values in this layer is not apparent. With the exception of a few scattered trees and buildings, this sector contains a relatively smooth landscape up to 500 m from the tower.

Figure 17 also contains fewer calculated values of  $z_0$  and  $u_*$  than were possible at the lowest levels. This is because the shear between levels 2 and 3 during this period more frequently failed to meet the minimum criterion of  $0.5 \text{ ms}^{-1}$ . For this reason, wind levels 3 and 4 of Tower 0006 (likewise for Tower 0110 in the following section), that contain even more such exclusions, are not shown here for the coastal wind cases.

Figure 18 clearly demonstrates the relationship between  $z_0$  and wind direction in varying stability conditions at the two lowest wind "layers" of Tower 0006. It contains polar plots of  $z_0$  averaged over  $15^\circ$  sectors for the entire year 2008 for the southeast sensors at levels 1 and 2 (Figure 18a) and levels 2 and 3 (Figure 18b). The tower location is the pole for these plots, and wind direction is the azimuthal coordinate. Line segments connecting the average  $z_0$  value (plotted on the center radials of each  $15^\circ$  sector) form the blue outline in each plot. Like the time series presented in this study, for all polar plots presented herein, in addition to averaging all variables over 20 minutes,  $z_0$  was not calculated for wind speeds less than  $2 \text{ ms}^{-1}$ .

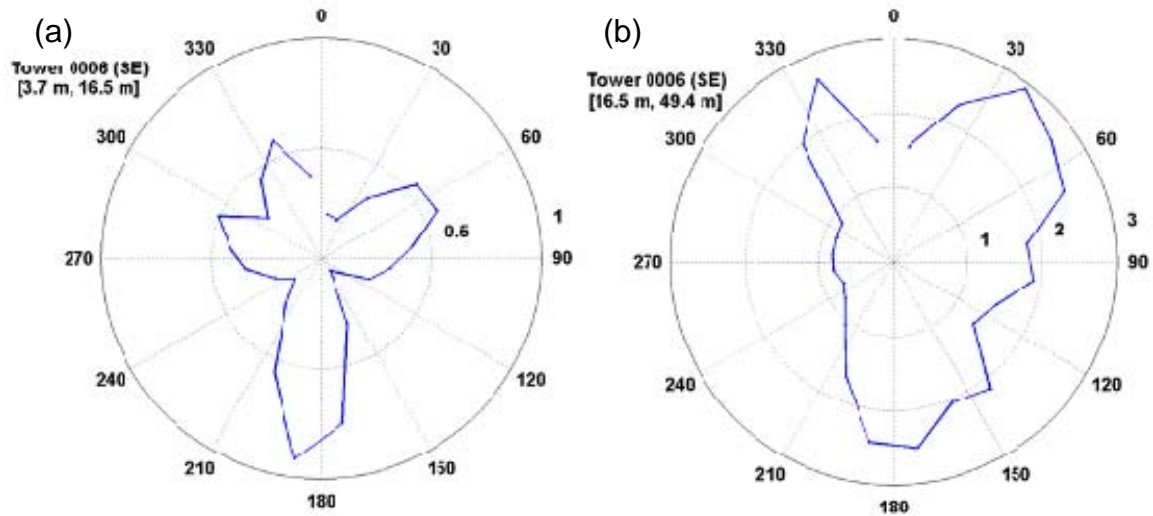


Figure 18. Azimuthal variation of calculated roughness length  $z_0$  averaged over each 15° sector from the southeast sensors at (a) wind levels 1 and 2 and (b) wind levels 2 and 3 of Tower 0006 for 1 January to 31 December 2008.

These " $z_0$  roses" compare reasonably well to the satellite images of Tower 0006 (Figures 13 and 14). In Figure 18a, the "X" pattern is discernible, though the branches of the "X" in the polar plot correspond to larger  $z_0$  values associated with areas of trees and shrubs between the cleared areas visible on the satellite photograph. In Figure 18b, sectors with larger  $z_0$  correspond to wind directions from forested areas situated 100–300 m from the tower. At the same distance to the west, the landscape appears to be smoother, and  $z_0$  values corresponding to westerly winds are lower.

## 2. Tower 0110

Tower 0110, a launch critical tower housing instrumentation at the same levels as Tower 0006, is located approximately 1.7 km from the shoreline (Figures 3 and 37) and 7 km NNW of Tower 0006. The eastern shore of the Banana River (actually a large brackish lagoon) is about 50 m west of the tower. At higher magnification (Figure 20), trees are visible between the tower and the Banana River, and trees are also present in sectors 160°–200° along the

riverbank and across Titan III Road to the east. Shadow analysis suggests the largest trees in the immediate vicinity are those located 25–50 m west-southwest of the tower along the riverbank. The smoothest sector in the immediate vicinity of the tower is that containing the tower's access road along radial 100° and the southeast branch of the "X." The surface in this sector appears relatively smooth to a distance of about 75 m.



Figure 19. Satellite photograph of Tower 0110 and surrounding area. Red "X" marks the tower location. Image ©2010 Google.



Figure 20. Satellite photograph of Tower 0110 and immediate surroundings. Red "X" marks the tower location. Image ©2010 Google.

Figures 21 and 22 are time series showing observations and calculated quantities from the southeast sensors at levels 1 and 2 of Tower 0110 on 1–4 June 2008. As observed at Tower 0006, SBFs occur before noon each day with similar responses in observed variables. In Figures 22a and 22b, secondary circulations (indicated by purple arrows), apparently influenced by the Banana River (Laird et al. 1995), are observed around sunrise each day as about a  $45^\circ$  veering in wind direction and a slight increase in  $q$ . Wind speeds decrease at night as with Tower 0006, though winds at Tower 0110 remain stronger on average throughout the period, possibly enhanced by divergence over the Banana River. In Figure 22c,  $z_0$  values less than 0.25 m are calculated in the afternoons following the SBFs, during which periods the wind direction is mostly from sector  $110^\circ$ – $140^\circ$ . As at Tower 0006, the  $z_0$  response at this layer appears to be due to the smooth surface near the tower in that direction.



Roughness lengths are greater (about 0.3–0.5 m) during two periods of southerly wind at speeds of 3–5  $\text{ms}^{-1}$ , one just before midnight on day 153 and one between midnight and sunrise on day 155. In this sector, tree density is relatively high, and the larger  $z_0$  values appear to be a direct result of flow over this denser forest canopy.

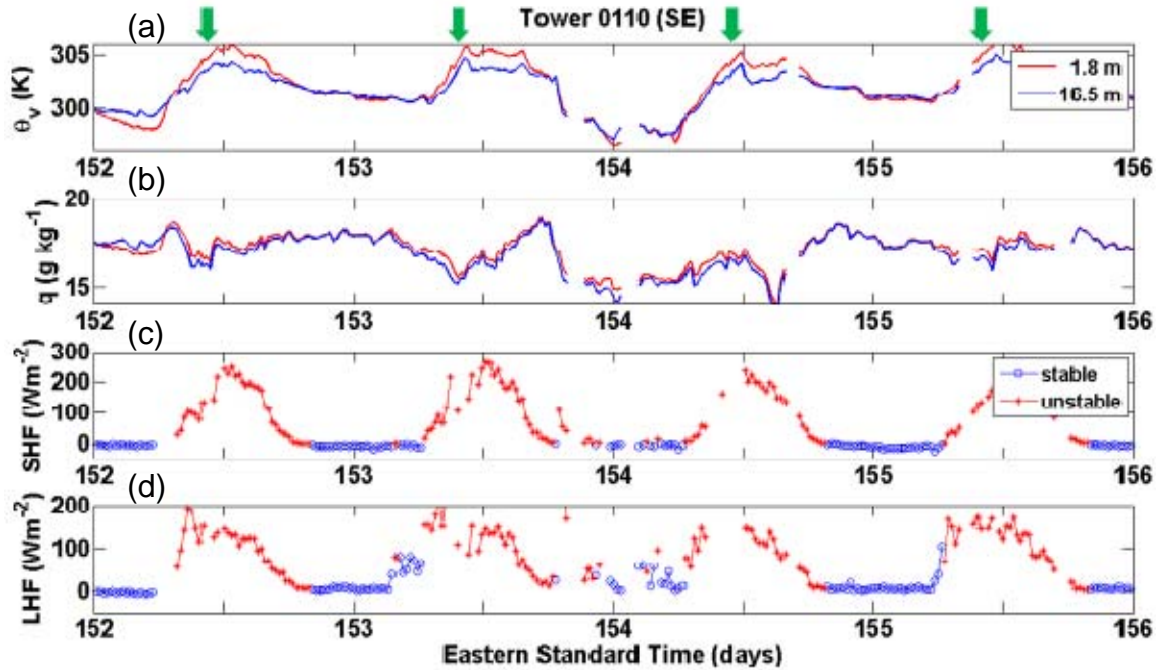


Figure 21. Same as Figure 6, except observed conditions and calculated quantities are from the southeast sensors at temperature levels 1 and 2 of Tower 0110 on 1–4 June 2008.

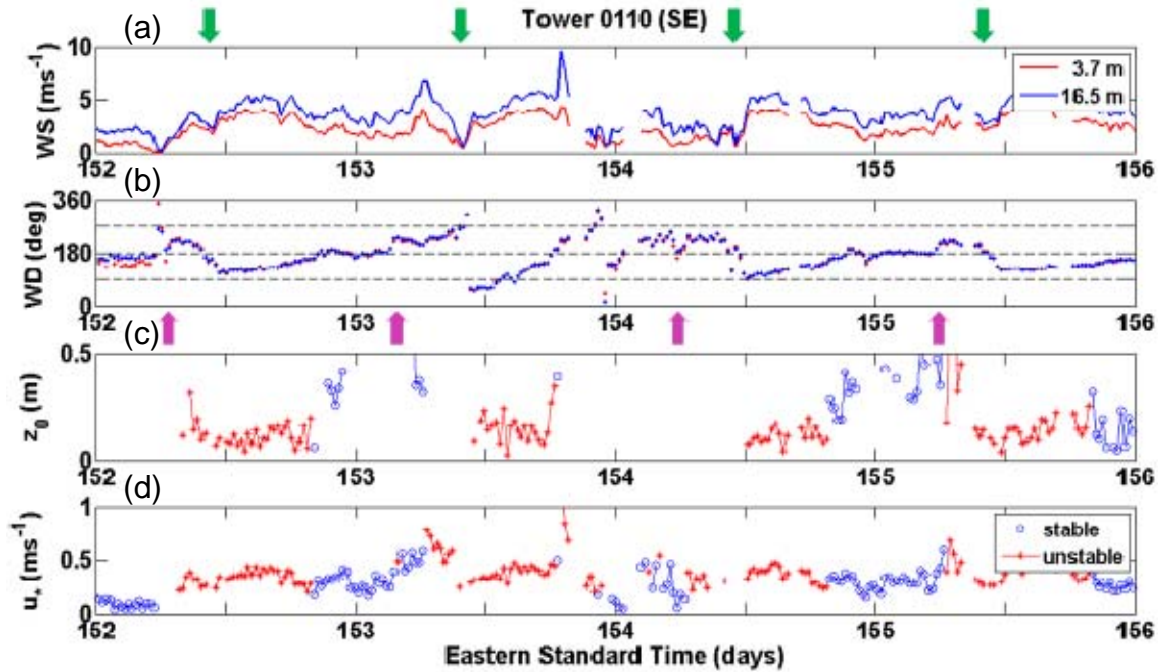


Figure 22. Same as Figure 7, except observed conditions and calculated quantities are from the southeast sensors at wind levels 1 and 2 of Tower 0110 on 1–4 June 2008.

Figure 23 is similar to Figure 22, but for wind levels 2 and 3 of Tower 0110. In this layer, as the flow veers from about  $120^\circ$  to  $170^\circ$  following each SBF passage,  $z_0$  values increase from about 0.5 m to 1.5 m. Two very brief periods during which the wind speed exceeded  $5 \text{ ms}^{-1}$  under southwesterly flow are observed just after sunrise on days 153 and 155 following the passage of the secondary circulations associated with the Banana River (purple arrows). During these periods,  $z_0$  values fall to less than 0.2 m. These low roughness lengths are an apparent response to flow over the smooth surface of the Banana River. Due to the intervening trees west of the tower and their role in the formation of an IBL, the Banana River was not "seen" in calculations of  $z_0$  at levels 1 and 2 from any wind sector.

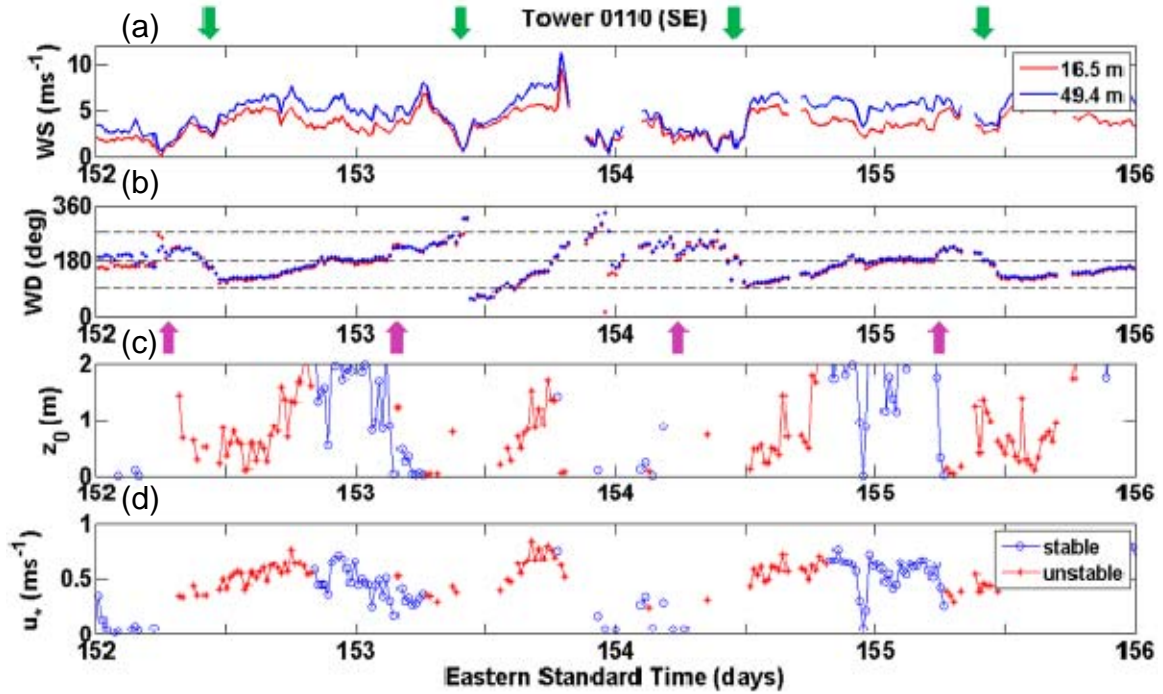


Figure 23. Same as Figure 7, except observed conditions and calculated quantities are from the southeast sensors at wind levels 2 and 3 of Tower 0110 on 1–4 June 2008.

Figure 24 contains " $z_0$  roses" for Tower 0110 for the lowest two layers of Tower 0110 for the entire year 2008. At the lowest layer (Figure 24a), the familiar branches of the "X" are present, and a lobe of  $z_0$  values exceeding 2 m is located in sector  $250^\circ$ – $280^\circ$ . As seen in Figure 20, this sector contains trees located between the tower and the Banana River. Between the 16.5-m and 49.4-m wind levels (Figure 24b), the IBL formed by these trees is not as prevalent, and flow from this sector corresponds to lower  $z_0$  values.

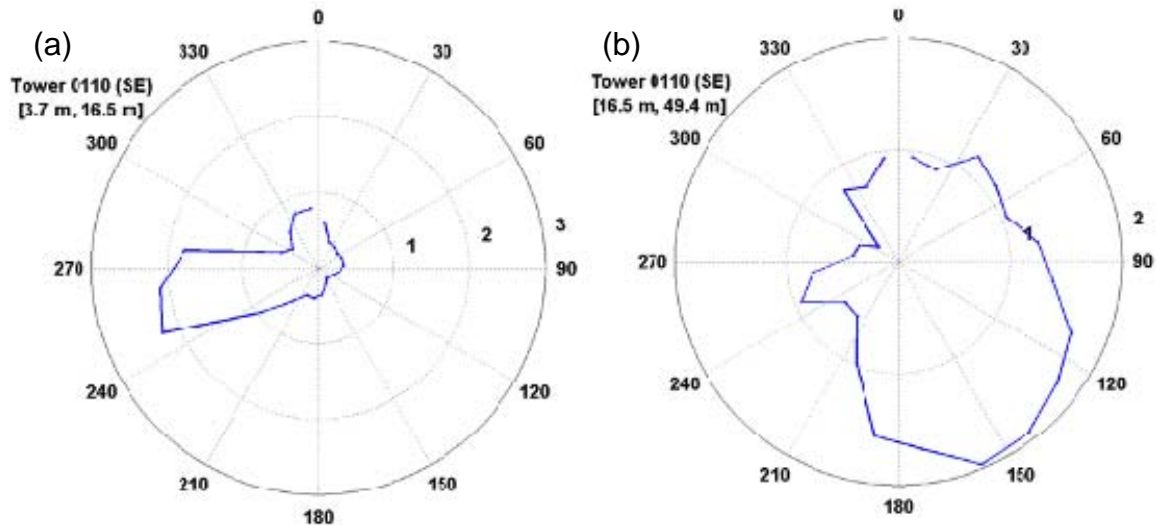


Figure 24. Azimuthal variation of calculated roughness length  $z_0$  averaged over each 15° sector from the southeast sensors at (a) wind levels 1 and 2 and (b) wind levels 2 and 3 of Tower 0110 for 1 January to 31 December 2008.

## B. ROUGHNESS LENGTH VARIATION IN RESPONSE TO TROPICAL STORM FAY

As discussed in Chapter III, the passage of Tropical Storm Fay near CCAFS on 20–21 August 2008 provided an ideal set of observations for consideration in this study. Launch critical towers 0002 and 0110 were selected for analysis of the roughness length response during Tropical Storm Fay.

### 1. Tower 0002

Tower 0002 is located approximately 700 m from the coastline (Figure 25). At higher magnification (Figure 26), the surface within a 150-m radius of the tower is fairly uniform, consisting mainly of shrubs and small trees except for the familiar "X" pattern and an effectively elongated southeast branch of the "X" aligned with the tower's access road along radial 140°. Qualitative shadow analysis reveals the largest trees in the area around Tower 0002 lie about 200 m distant in sector 250°–330°. At a radius of about 300–500 m, the surface is somewhat smoother, both along the immediate shoreline to the southeast and on cleared land containing scattered buildings and structures to the west.





Figure 25. Satellite photograph of Tower 0002 and surrounding area. Red "X" marks the tower location. Image ©2010 Google.



Figure 26. Satellite photograph of Tower 0002 and immediate surroundings. Red "X" marks the tower location. Image ©2010 Google.

Figures 27 and 28 are time series showing measurements and calculated quantities from the southeast sensors at levels 1 and 2 of Tower 0002 on 18–21 August 2008. In Figure 27, diurnal variation of the surface-layer temperature and

heat fluxes are clearly seen on day 230 but become obscured on the remaining days because of cloud cover and precipitation associated with Fay. On days 231–234, the surface layer is slightly unstable, SHF averages  $50 \text{ Wm}^{-2}$ , and LHF averages  $100 \text{ Wm}^{-2}$ . Near the end of the period, the level-1 temperature and humidity sensors failed to record usable data, and as a result, calculations following the failure should be disregarded.

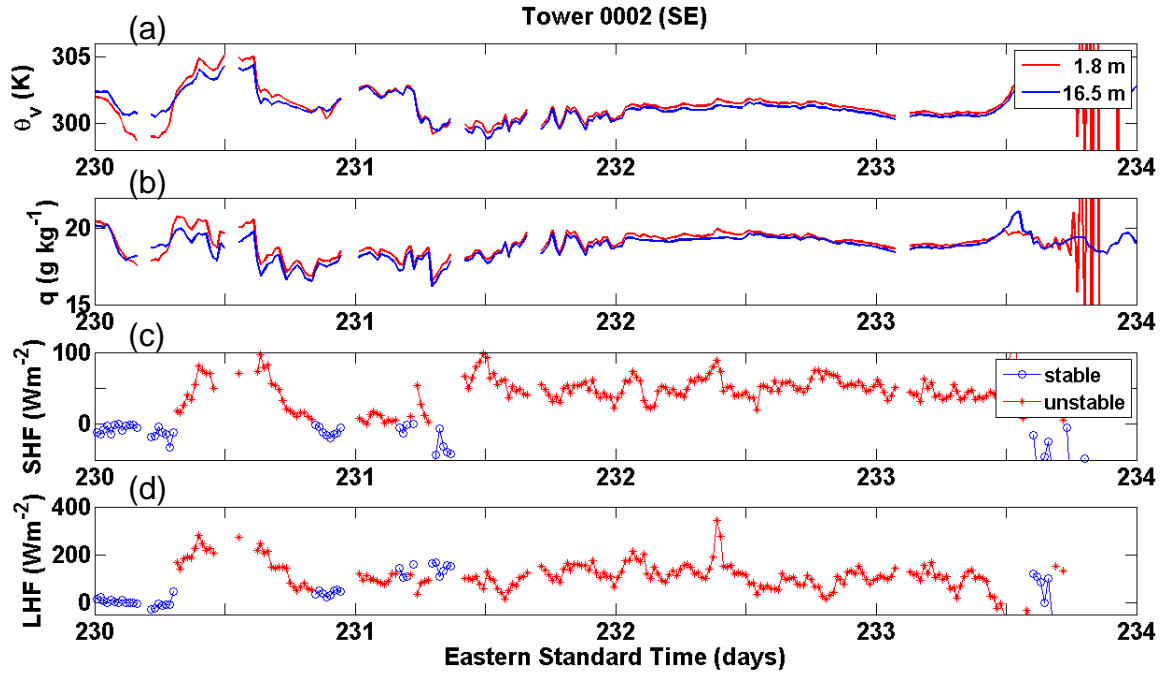


Figure 27. Same as Figure 6, except observed conditions and calculated quantities are from the southeast sensors at temperature levels 1 and 2 of Tower 0002 on 18–21 August 2008.

In Figure 28, as the center of Tropical Storm Fay approached CCAFS on days 230 and 231, the wind direction remained fairly consistent from the east and southeast and gradually increased in speed. With appreciable shear between wind levels 1 and 2,  $u_*$  also increased with wind speed as expected. On day 231, with a steady east wind,  $z_0$  values averaged 0.5 m, a reasonable magnitude given the numerous but separate small trees in that sector within 100–200 m of the tower (Figure 26). From midnight until noon on day 232, the wind direction veered at a fairly constant rate from easterly to westerly as the center of Fay

crossed the latitude of CCAFS. During this 12-hour period, with wind speeds exceeding  $10 \text{ ms}^{-1}$ ,  $z_0$  values sharply decreased to about 0.1 m when the wind direction was from sector  $120^\circ$ – $150^\circ$ , which corresponds closely to the sector containing the tower access road. By about sunrise (0600 EST), the wind direction had shifted more to the south and  $z_0$  increased, which is reasonable given the trees present in that sector. Around noon, a brief period of low  $z_0$  values is identifiable when the flow is from about radial  $220^\circ$ , which contains cleared ground along the southwest branch of the "X". After backing about  $60^\circ$ , the wind remains steady from about  $220^\circ$  on day 233 and calculated  $z_0$  values are slightly lower as a result of the relative smoothness of this sector within 50 m of the tower.

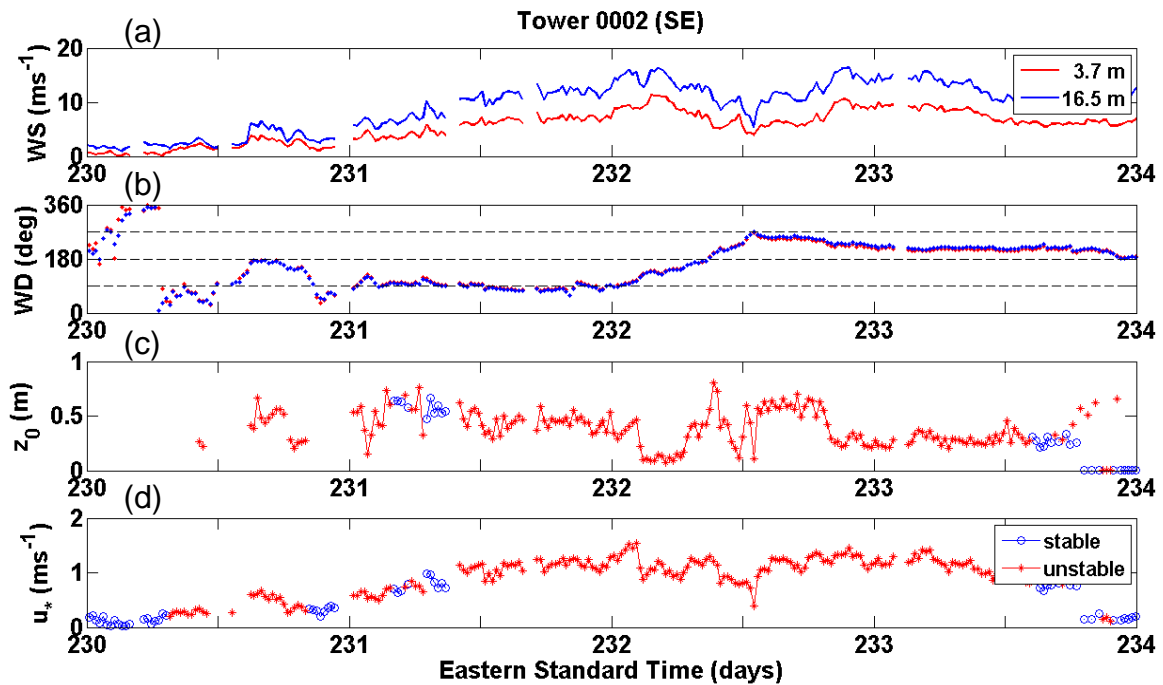


Figure 28. Same as Figure 7, except observed conditions and calculated quantities are from the southeast sensors at wind levels 1 and 2 of Tower 0002 on 18–21 August 2008.

Figure 29 shows measurements from the southeast sensors at wind levels 2 and 3 of Tower 0002 during Tropical Storm Fay. At these levels,  $z_0$  (calculated using thermal data from levels 1 and 2) averages above 1 m until just before

noon on day 232, when values sharply decrease. During this brief period of low  $z_0$  values (about 0.2 m), the flow is from sector 220°–240°. In addition to the "X" branch in this sector, cleared land southwest of the tower is closest (about 220 m) in this direction and may be contributing to the low  $z_0$ . If this is true, then this observation also demonstrates the dependence of  $z_0$  upon wind speed since lower speeds in the coastal wind circulation cases corresponded to  $z_0$  values indicative of shorter distances "seen" by wind levels 2 and 3.

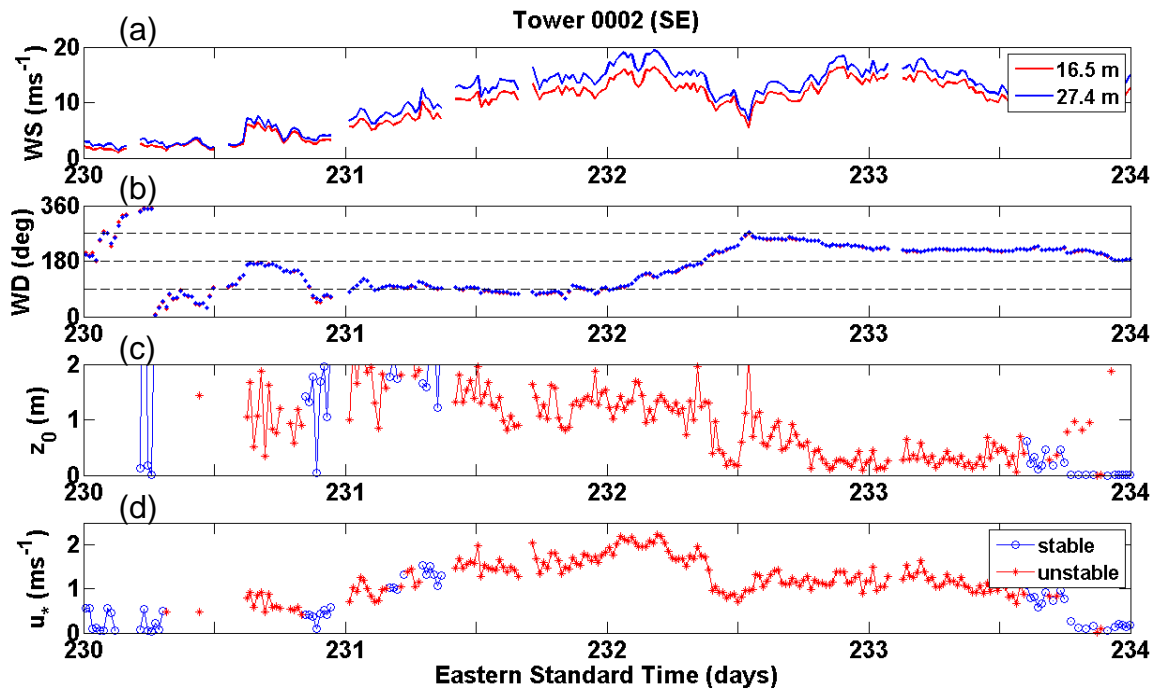


Figure 29. Same as Figure 7, except observed conditions and calculated quantities are from the southeast sensors at wind levels 2 and 3 of Tower 0002 on 18–21 August 2008.

Figures 30 and 31 are from the southeast sensors at temperature levels 2 and 3 and wind levels 4 and 5 of Tower 0002 during Tropical Storm Fay. The large gaps in the calculated values on day 230 are due to insufficient wind shear. In Figure 30, specific humidity at level 3 is suspect, since the trace of  $q$  at both levels is essentially parallel and the 16.5-m sensor averages  $2 \text{ g kg}^{-1}$  higher than the 62.2-m sensor. Such a large difference in specific humidity in less than 50 m seems unrealistic given the uniformity of the wind field. On day 233, temperature



and humidity fails to record at level 3, and calculated results thereafter are not reliable. Despite this questionable humidity data on days 230–233, confidence in  $z_0$  remains high since the effect of variations in stability is minimized when wind speed is stronger in near-neutral conditions, as noted in Chapter III.

In an attempt to both validate the hypothesis of this study and quantify the degree to which the distance "seen" by various tower layers varies with altitude and wind speed, it is tempting to search for evidence that Tower 0002 can "see" the ocean from observations at its highest levels. In Figure 31, from noon on day 231 to midnight on day 232, with a steady easterly wind,  $z_0$  values are between 1 m and 3 m. In this direction, as seen in Figure 32, the distance to the ocean is approximately 1.6 km. Once the wind direction begins to veer on day 232,  $z_0$  decreases to less than 0.5 m, remaining at about this value, while the flow is from sector 110°–180°. Such low roughness lengths in this sector could be caused by either the ocean (presumably roughened due to the tropical storm) or the sparse vegetation along the immediate shoreline, since the distance between the tower and the ocean is lowest in this sector.

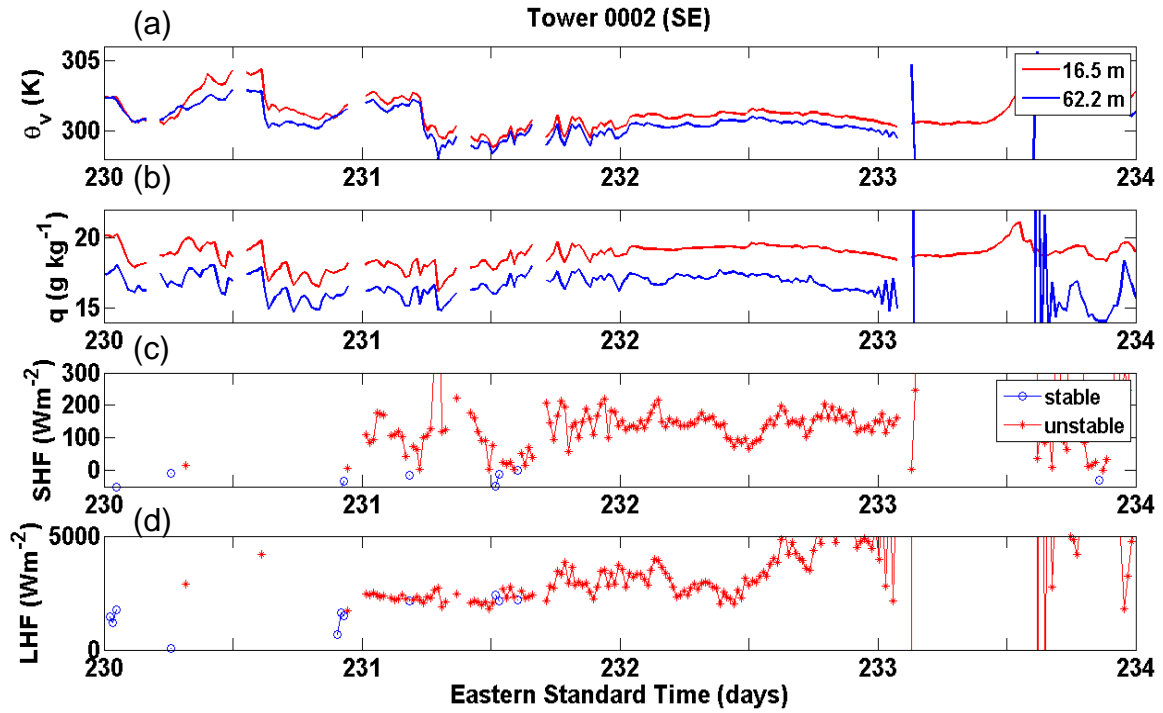


Figure 30. Same as Figure 6, except observed conditions and calculated quantities are from the southeast sensors at temperature levels 2 and 3 of Tower 0002 on 18–21 August 2008.

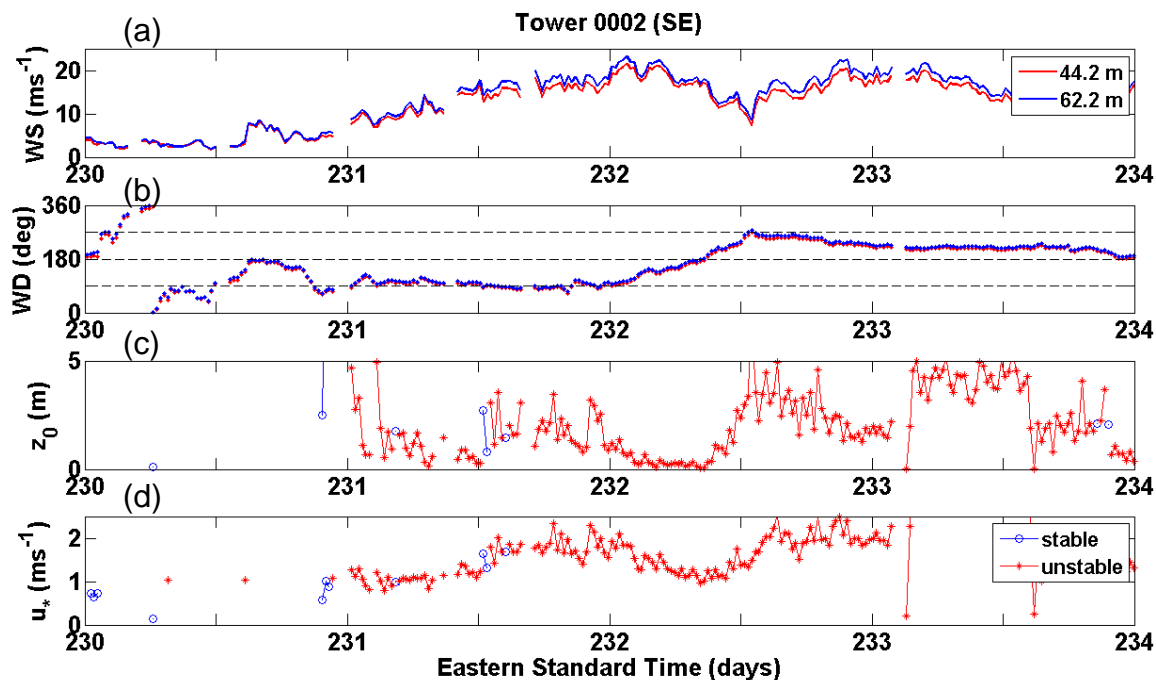


Figure 31. Same as Figure 7, except observed conditions and calculated quantities are from the southeast sensors at wind levels 4 and 5 of Tower 0002 on 18-21 August 2008.

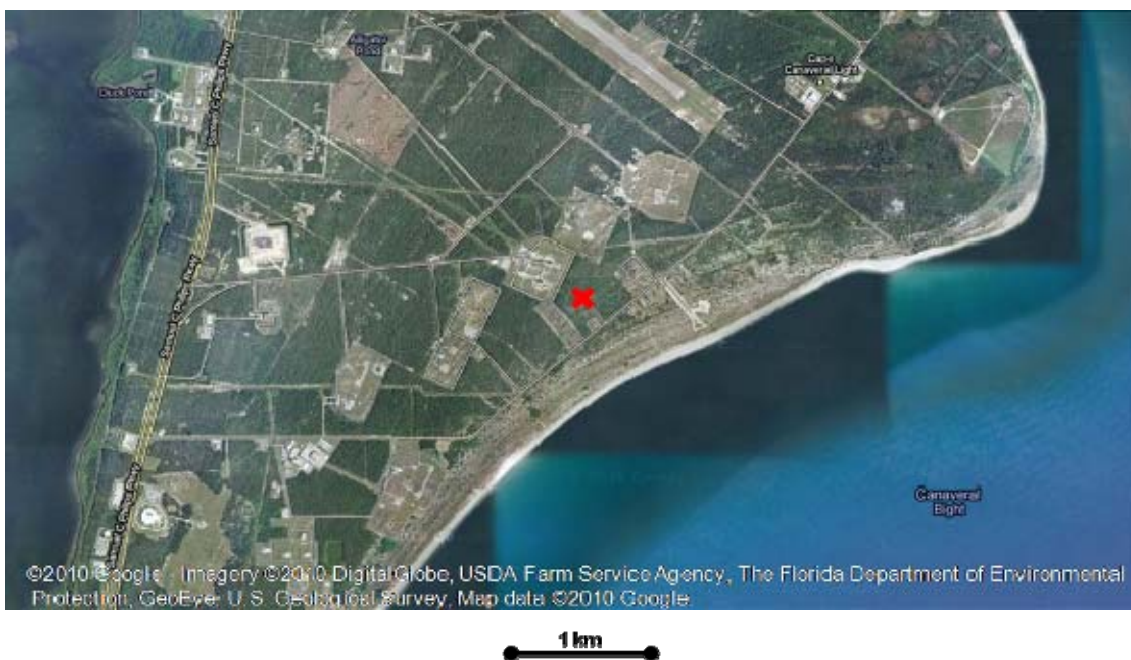


Figure 32. Satellite photograph showing the proximity of Tower 0002 to the Atlantic Ocean. The tower is less than 1 km from the ocean in sector  $120^{\circ}$ – $180^{\circ}$ . Red "X" marks the tower location. Image ©2010 Google.

Figure 33 contains polar plots of  $z_0$  for the lowest two layers of Tower 0002 for the entire year 2008. In Figure 33a, the lowest layer is again dominated by the "X" pattern, which is more uniform here than for Towers 0006 and 0110. In Figure 33b,  $z_0$  maxima in sector 260°–280° and along radial 320° correspond to trees about 200 m from the tower as previously noted. The decrease in  $z_0$  observed between these sectors corresponds to a gap in the trees visible in the upper left of Figure 26, which opens to cleared land beyond. Another relative minimum occurs in sector 220°–250°, which contains cleared land 200–300 m from the tower.

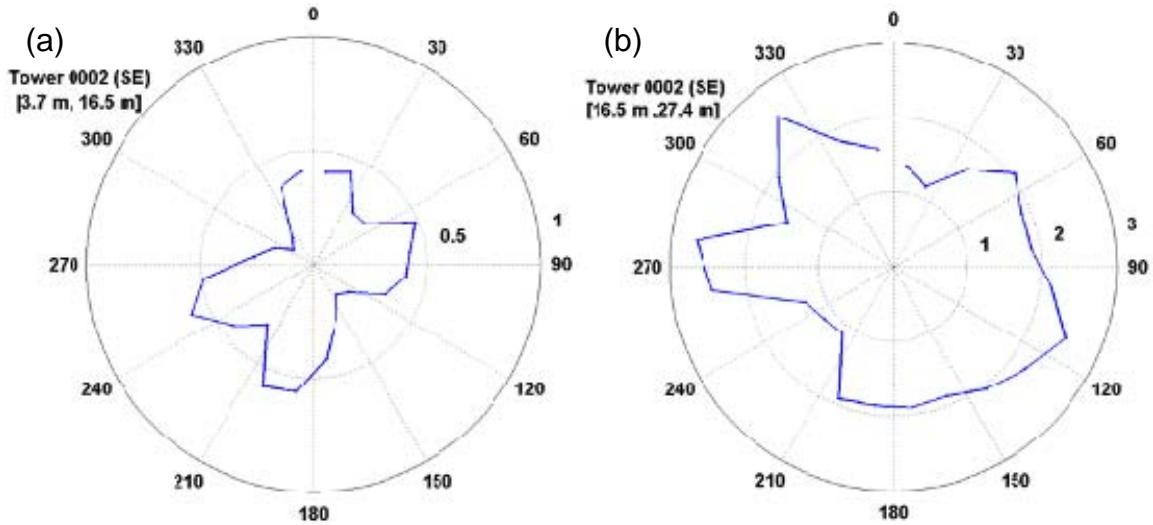


Figure 33. Azimuthal variation of calculated roughness length  $z_0$  averaged over each 15° sector from the southeast sensors at (a) wind levels 1 and 2 and (b) wind levels 2 and 3 of Tower 0002 for 1 January to 31 December 2008.

## 2. Tower 0110

In addition to the coastal wind circulation case, observations from Tower 0110 were also selected to evaluate the  $z_0$  response during Tropical Storm Fay. Satellite photographs of the tower are given in Figures 19 and 20. For this case, the extent to which the Banana River can be "seen" by the various levels of Tower 0110 and whether this effect differs from the coastal wind case are investigated.

Figures 34 and 35 are time series showing measurements and calculated quantities from the southeast sensors at levels 1 and 2 of Tower 0110 on 18–21 August 2008. In Figure 34, observations of temperature and humidity and the calculated heat fluxes at this location are similar to that of Tower 0002, located 16 km to the southeast. Just after midnight on day 232, the level 2 humidity sensor fails to record data but appears to recover on day 233. Again, this outage does not significantly affect the calculations for  $z_0$  due to the near-neutral conditions during this event.

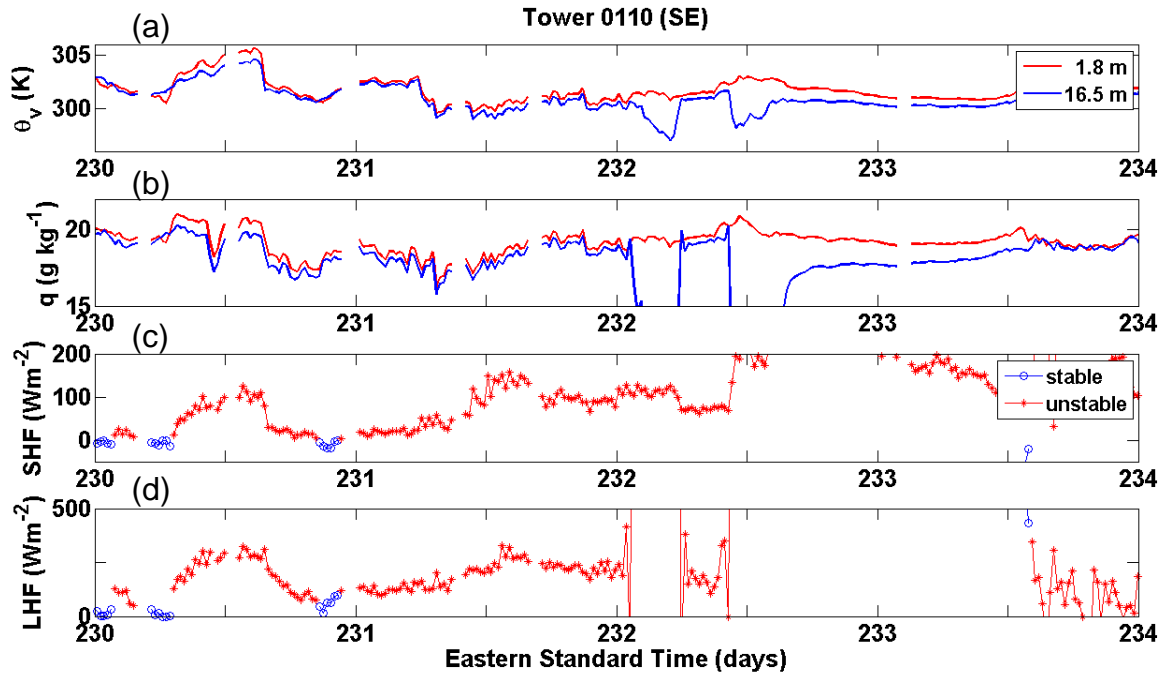


Figure 34. Same as Figure 6, except observed conditions and calculated quantities are from the southeast sensors at temperature levels 1 and 2 of Tower 0110 on 18–21 August 2008.

In Figure 35, the wind direction was from the east and southeast, and the wind speed steadily increased until the morning of day 232. Just before noon, as the center of Fay was near the tower, winds calmed and abruptly veered to the west in about 1 hour, a notable difference from the 12-hour wind shift observed at Tower 0002. On days 231 and 232, lower  $z_0$  values are calculated while the wind direction was from the east and southeast, a similar trend to the coastal

wind case. After the wind shift,  $z_0$  rapidly increases to over 2 m, which is reasonable given the wind speed and the proximity of the trees west of the tower.

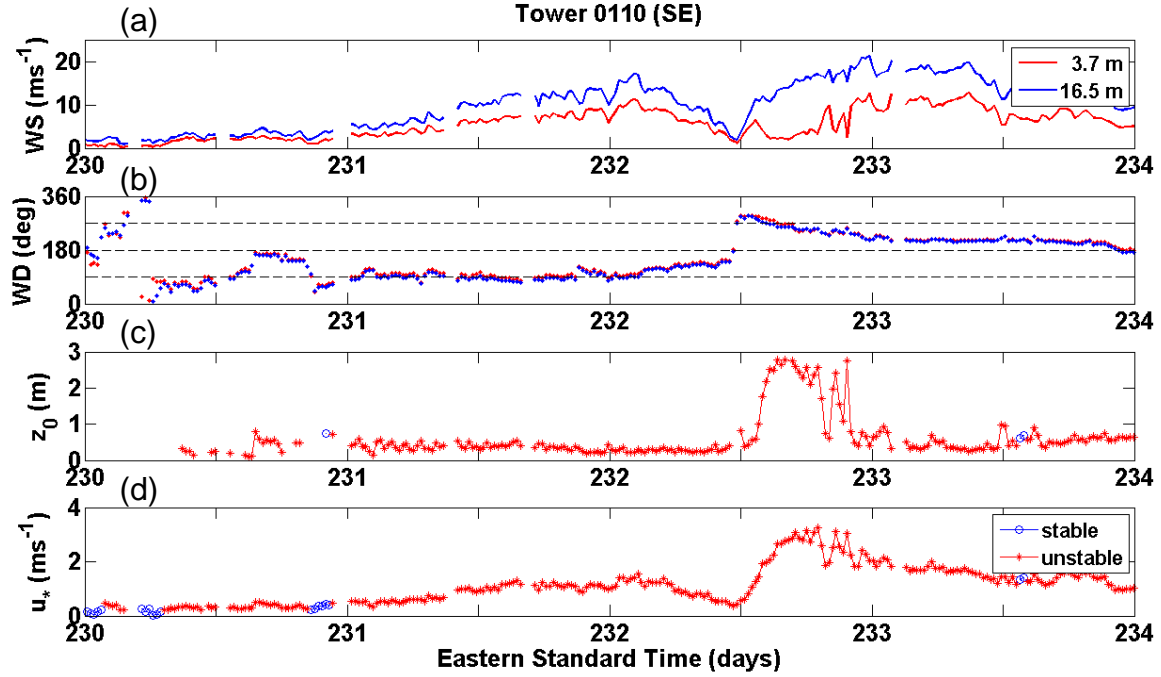


Figure 35. Same as Figure 7, except observed conditions and calculated quantities are from the southeast sensors at wind levels 1 and 2 of Tower 0110 on 18–21 August 2008.

Figure 36 shows observed and calculated values from wind levels 2 and 3 of Tower 0110 during Tropical Storm Fay. At these levels,  $z_0$  (calculated using thermal data from levels 1 and 2) rapidly decreases at the time of the wind shift. Corresponding to flow from the east and southeast,  $z_0$  values averaged above 1 m, while after the shift,  $z_0$  values fall to 0.05 m, indicative of flow over the very smooth surface of the Banana River. Near the end of the period, the wind direction has backed to about  $180^\circ$ , and  $z_0$  values increase as a result of the fetch over forested land. Comparing Figures 23 and 36, it is possible to discern a similar effect in the  $z_0$  response at wind levels 2 and 3 in both the coastal wind and Fay cases, although fewer observations of wind from the direction of the River were recorded for the coastal wind case.

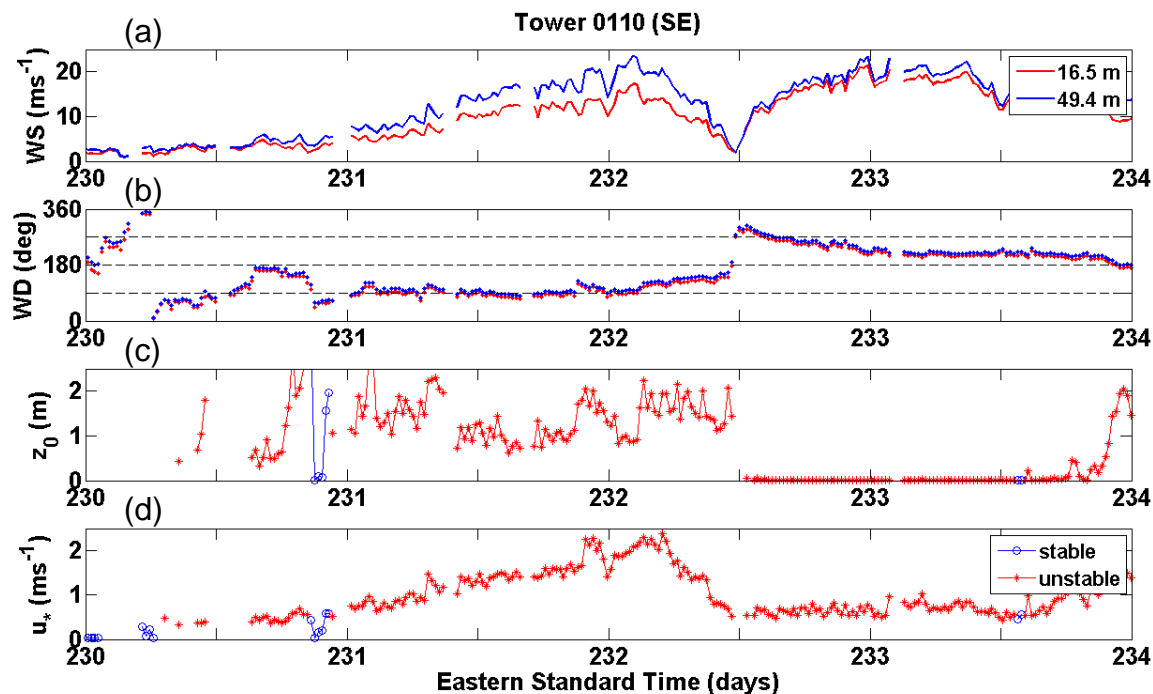


Figure 36. Same as Figure 7, except observed conditions and calculated quantities are from the southeast sensors at wind levels 2 and 3 of Tower 0110 on 18–21 August 2008.



Figure 37. Satellite photograph showing the proximity of Tower 0110 to the Banana River and Atlantic Ocean. Red "X" marks the tower location. Image ©2010 Google.



In Figure 37, the west to southwest wind sector following the shift has a 1–2 km fetch across the Banana River, and the very low  $z_0$  values in Figure 35 confirm that wind levels 2 and 3 can "see" this fetch, while levels 1 and 2 sense the IBL induced by the trees along the riverbank.

Figures 38 and 39 are time series of observed and calculated values from temperature levels 2 and 3 and wind levels 3 and 4 of Tower 0110 during Tropical Storm Fay. As observed at the upper levels of Tower 0002, lower shear at these levels results in more gaps in the calculated quantities on both figures. Although relatively few data points for  $z_0$  are present on day 233, they are of similar magnitude to those observed at wind levels 2 and 3 and support the conclusion that these low roughness lengths result from flow across the Banana River.

Before sunrise on day 232 and near the time of the maximum observed wind speed of  $25 \text{ ms}^{-1}$ , a second period of low  $z_0$  values correspond to a wind direction of about  $120^\circ$ . Along this radial, areas of trees and the northern edge of cleared land around the Mars Observer Launch Facility (Figure 37, lower right) lie between the tower and the ocean, which is about 2 km from the tower. It is tempting to attribute this period of low  $z_0$  values to the ocean, particularly given the high wind speed, but if this were true, then when the winds were from the east and even stronger a few hours earlier (about midnight),  $z_0$  should have also been low, since in this direction the tower is only about 1.5 km from the shoreline. An additional factor is the level 2 humidity sensor failure during this time, which results in an unrealistic stability profile and has a minor effect on the magnitude (though not the trend) of  $z_0$ . The effect of backing winds due to increased frictional drag over land was considered, but any correction for this effect would require that the  $120^\circ$ – $140^\circ$  flow observed at the tower corresponding to the low  $z_0$  values in the early morning hours of day 232 would have a greater southerly—not easterly—component, hence an even longer fetch over land. In this case, a



more reasonable conclusion is that the low  $z_0$  values in the early morning hours of day 232 are probably a result of flow over the cleared land around the Mars Observer Launch Facility.

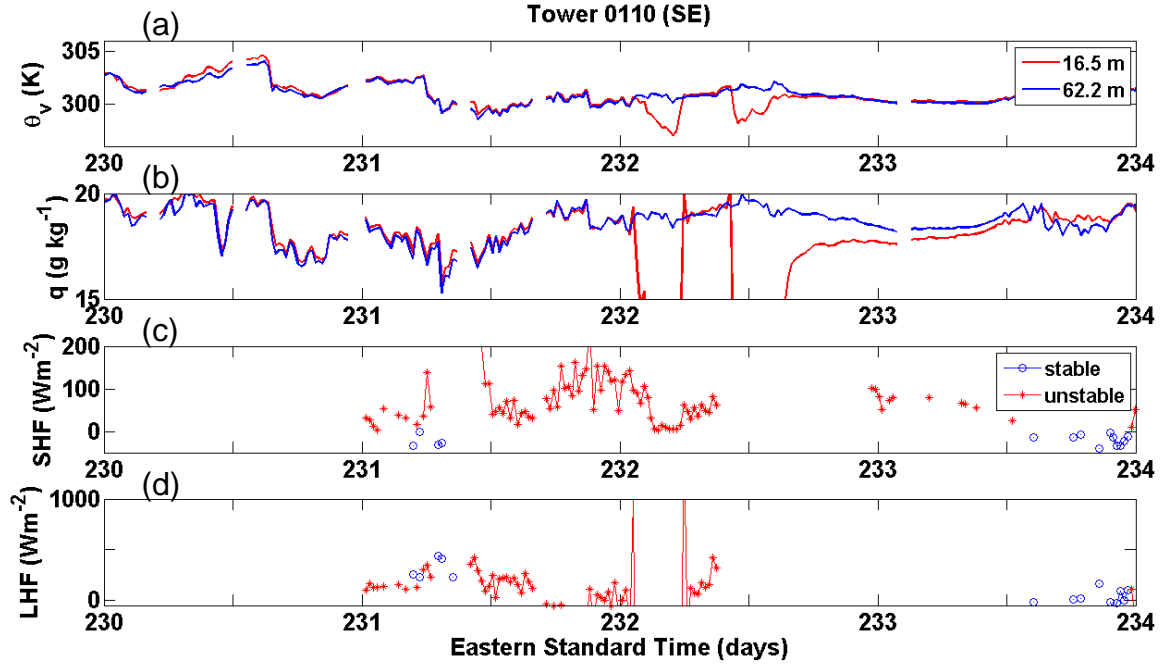


Figure 38. Same as Figure 6, except observed conditions and calculated quantities are from the southeast sensors at temperature levels 2 and 3 of Tower 0110 on 18–21 August 2008.

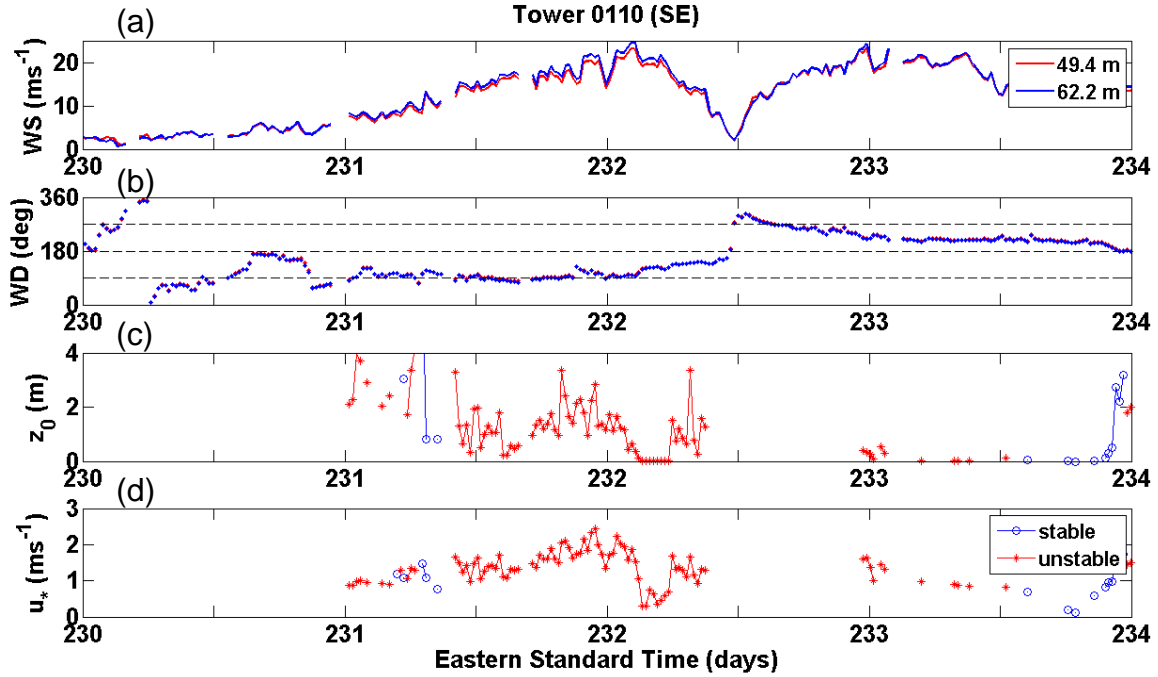


Figure 39. Same as Figure 7, except observed conditions and calculated quantities are from the southeast sensors at wind levels 3 and 4 of Tower 0110 on 18–21 August 2008.

### C. ROUGHNESS LENGTH FROM DIFFERENT OBSERVATION LEVELS

Figures 40 and 41 are time series of wind conditions and roughness lengths calculated from observations at various combinations of levels of Tower 0002 on 23–25 September 2008. Though this period is not included in the cases discussed earlier in this chapter, the variation in  $z_0$  shown here demonstrates the multi-layer structure of the surface layer in the region.

Figure 40 shows the wind direction and wind speed from the northwest sensors at the lowest two wind levels of Tower 0002 on 23–25 September 2008. During this two-day period, the wind direction was from the northeast with speeds of 5–8  $\text{ms}^{-1}$ . Figure 41 shows the roughness length calculated from different combinations of wind level and temperature level pairs. In the legend, SE12/12 indicates that  $z_0$  is calculated for the southeast sensors using observations at wind levels 1 and 2 (the digits before the solidus) and temperature levels 1 and 2. Three groups of roughness length variations are observed:  $z_0$  from the lowest

two levels, the middle levels, and the upper levels. Values of  $z_0$  for the lowest layer (blue) are on average the smallest, with a mean roughness length in this layer of about 0.5 m. Roughness length from the top layer, between 44.2 and 62.2 m (magenta), has values of over 4 m and a large temporal variation. It is likely that these two levels are usually above the surface layer, and thus  $z_0$  calculated from Monin-Obukhov theory is not valid. Results from the various combinations of the middle levels are consistent with each other but differences are noted between the middle levels and the lowest layer. These results suggest that the lowest two levels are probably within the IBL induced by roughness elements in the immediate vicinity, while the middle levels sense the boundary layer advected by the northeast winds. The relatively small roughness length calculated for the lowest layer is consistent with the smooth surface along the northeast branch of the "X." At higher levels, sensors observed turbulent eddies induced by trees and shrubs farther to the northeast.

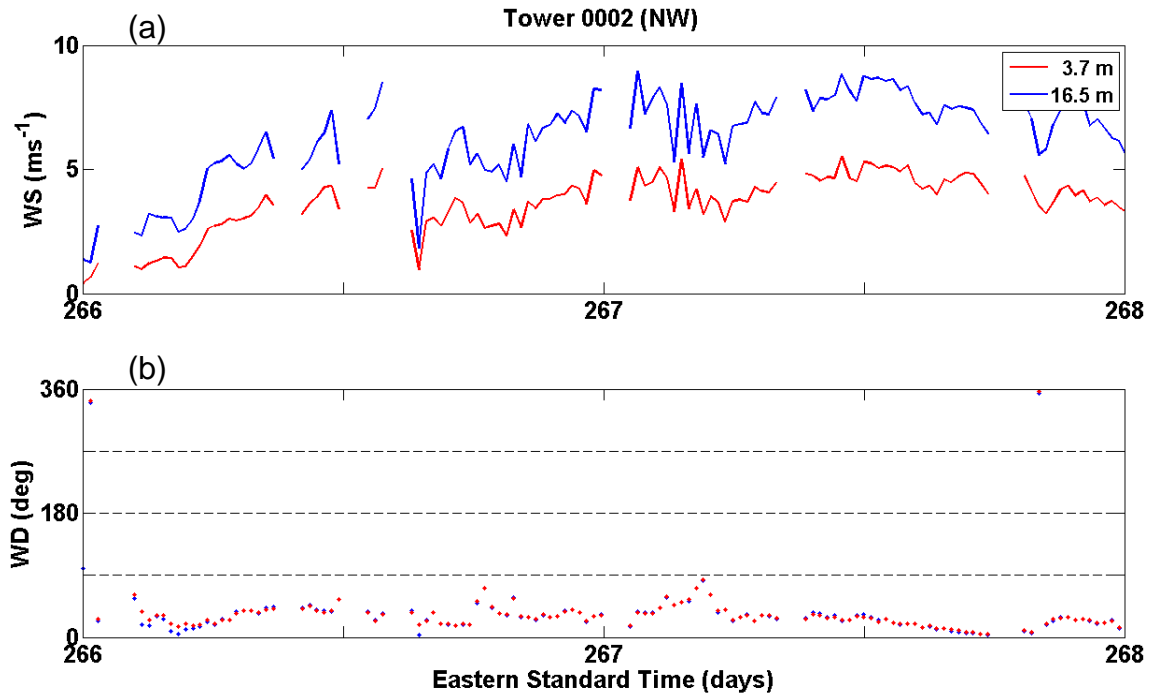


Figure 40. Temporal variation of observed (a) wind speed and (b) wind direction from the northwest sensors at wind levels 1 and 2 of Tower 0002 on 23–25 September 2008.

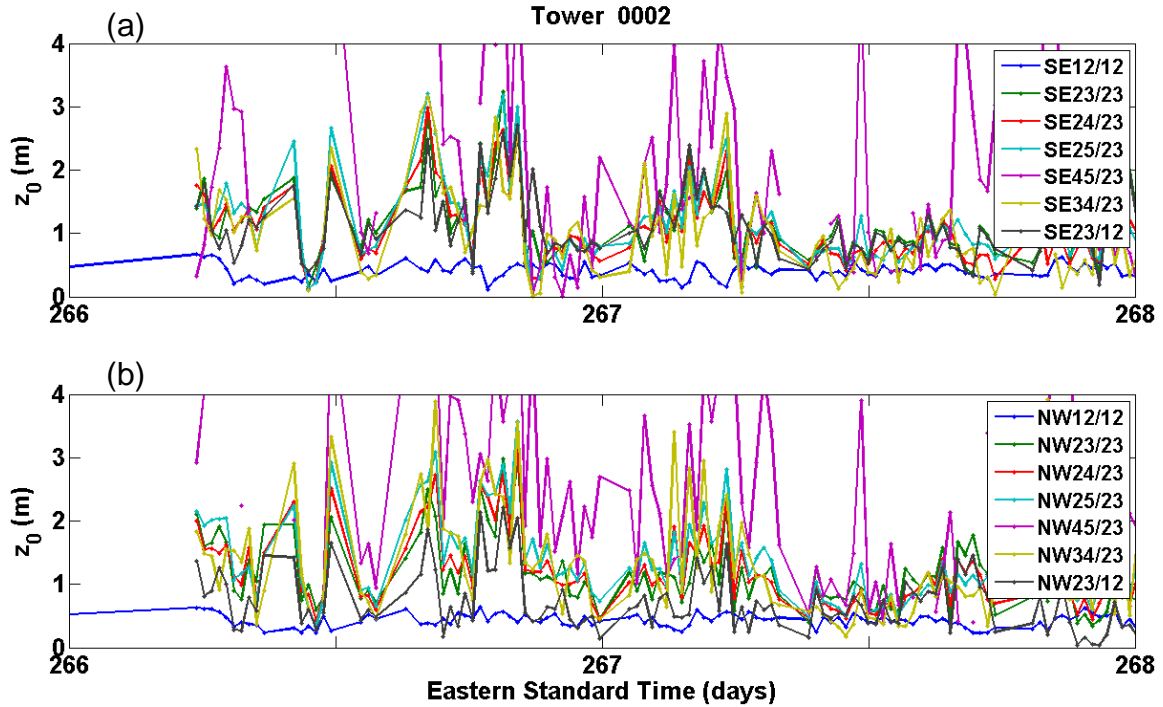


Figure 41. Temporal variation of calculated roughness lengths at various combinations of level pairs from (a) the southeast sensors and (b) the northwest sensors of Tower 0002 on 23–25 September 2008.

During most of the daylight hours of day 267, when wind speeds were at their highest,  $z_0$  values from all layer combinations are relatively uniform in magnitude and suggest that flow during this period did not exhibit multiple IBLs. This period corresponds to a wind direction roughly aligned with the northeast branch of the “X” at this tower. During periods in which the wind profile has a multiple IBL structure, Monin-Obukhov theory must be applied with caution in order to avoid crossing from one layer to another. Doing so would invalidate the “constant-flux” approximation, since each IBL is in effect a separate surface layer. A method of correction for this issue was not applied to the calculations in this study, but is worthy of consideration in future work.

Moreover, Figure 41 shows the temporal variation in  $z_0$  from both the northwest and southeast sensors. During this period the wind direction is from the northeast. Therefore, flow distortion caused by the tower does not

significantly influence the calculation of  $z_0$  from sensors on either side of the tower. Hence, the calculated results from both sets of sensors are very consistent.

## V. CONCLUSION

### A. SUMMARY OF RESULTS

In this study, near-surface observations are examined to determine relationships between surface characteristics and the temporal response of roughness length  $z_0$  from various altitudes. Although the WINDS sensors are capable of measuring and recording observations at higher accuracy, relatively imprecise measurements were available for this study—particularly the wind speed data—that were given in integer knots. Nevertheless, after averaging the observations over 20 minutes to better represent mean conditions, reasonable values for surface fluxes and roughness lengths were calculated using the WINDS data for various stability conditions when wind speed exceeded  $2 \text{ ms}^{-1}$ . In low wind conditions, the coarse precision of the data together with inherent uncertainties in Monin-Obukhov similarity theory for free convective conditions resulted in unphysically large values and temporal variations in the calculated roughness lengths. To mitigate these effects, observations taken at low wind speed, which occurred most frequently in the nocturnal stable surface layer, were excluded from the calculations.

Two periods suitable for the intended analysis were identified, coastal wind circulations on 1–4 June 2008 and Tropical Storm Fay on 18–21 August 2008. In the coastal wind case, the sudden change in wind direction following the passage of SBFs provided an ideal scenario to evaluate the variation of roughness length with wind direction. During the tropical storm, high wind conditions minimized the relative error due to the precision of the wind speed measurement, thus increasing confidence in the calculated surface-layer fluxes and roughness lengths.

Results revealed significant variation in  $z_0$  consistent with upstream roughness elements to a distance of about 100 m to 2 km, which varied with wind speed and observation height. Lower observation levels of the tower were often

located within IBLs induced by the surface in the immediate vicinity of the tower that limited the upwind distance roughness characteristics could be sensed, even in stronger winds.

Ultimately, the goal of this and similar research is to develop improved methods to incorporate the dependence of turbulent fluxes upon the ABL wind field in mesoscale numerical weather models. To illustrate the potential implications of this dependence, Figure 42 compares observed and calculated data from the WINDS to the Coupled Ocean/Atmosphere Mesoscale Prediction System (COAMPS) model fields for selected times during Tropical Storm Fay.

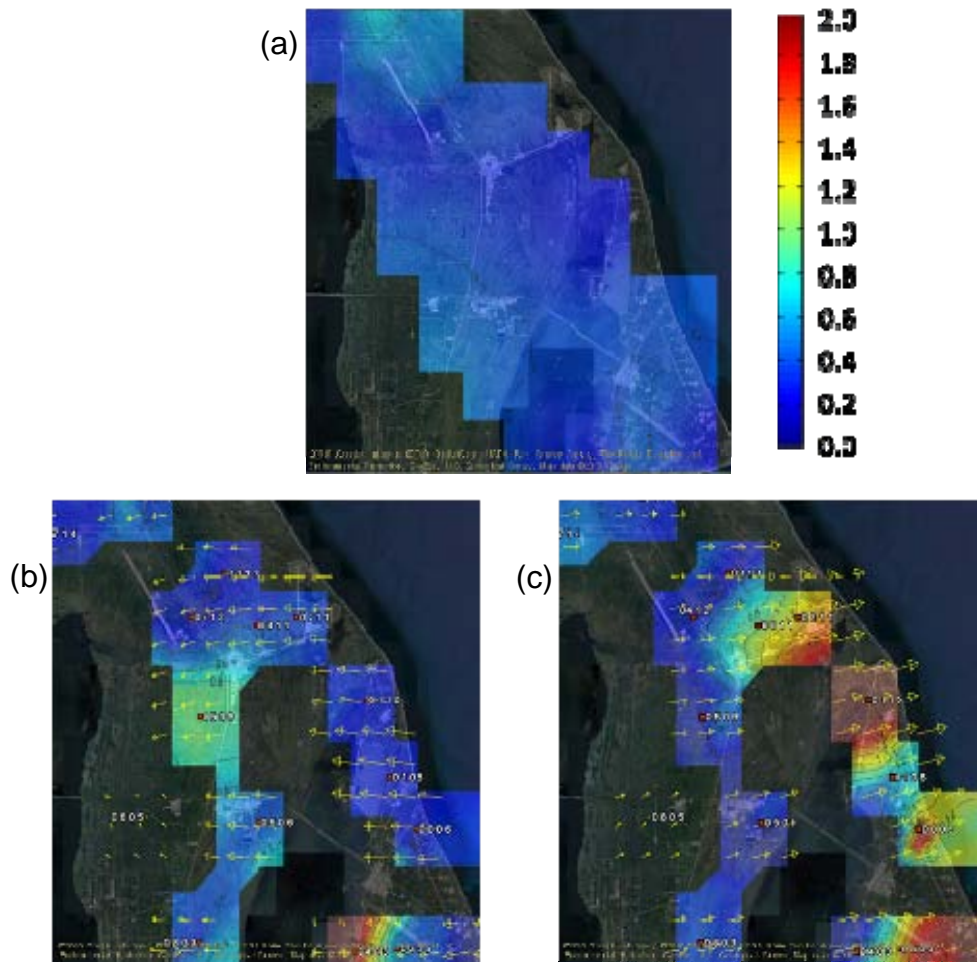


Figure 42. Contoured roughness length from (a) COAMPS and 16.5-m wind observations and calculated  $z_0$  from the WINDS at (b) 0000 EST and (c) 1800 EST on 20 August 2008. COAMPS data courtesy of the Naval Research Laboratory; image ©2010 Google.

In Figure 42, satellite imagery of the Cape Canaveral region is overlain by interpolated  $z_0$  values contoured at 0.2 m intervals. As previously noted,  $z_0$  is a fixed quantity at each grid point in mesoscale models, including COAMPS. Figure 42a is the constant COAMPS  $z_0$  field. Across this region, COAMPS  $z_0$  values are uniformly low, ranging from about 0.2–0.6 m (see color scale). Roughness height over the surface of the Banana River is assigned a suitably low value, within the limit of model resolution. At the resolution of COAMPS, subgrid-scale surface heterogeneities such as those considered in this study are not discernible. Figure 42b is a contour plot of  $z_0$  (using observations from the lowest two tower levels) at about 0000 EST on 20 August 2008, when the center of Fay was located southwest of CCAFS. Arrows indicate the speed and direction of the 16.5-m wind. Figure 42c is a contour plot of winds and  $z_0$  from 18 hours later, when Fay had moved northeast of CCAFS and winds were offshore. The earlier image shows that for WINDS locations near the coast,  $z_0$  values were comparable to the fixed COAMPS  $z_0$  field in the strong onshore flow conditions. In the later image, with a strong offshore flow component and about the same wind speeds, areas of higher  $z_0$  values are present. An area in the center of both plots was excluded in order to avoid interpolating across a large area devoid of observations.

Compared to the COAMPS gridded data field, relatively few observation sites were used to construct these contour plots; however, values near the higher-density tower locations carry a high degree of confidence, such as those along the immediate coastline and in the cluster of towers located at the top of the images. The observed temporal and spatial variation of roughness length is not represented by COAMPS, which depends upon land surface type only and is independent of wind flow. Relating the roughness length to the surface-layer dynamics would involve a complex blending of the effects of various IBLs over heterogeneous regions, and this relationship would be necessarily dependent upon wind speed and direction.



## **B. RECOMMENDATIONS FOR FUTURE RESEARCH USING THE WINDS OBSERVATIONS**

Wind speed observations with a precision of about  $0.05 \text{ ms}^{-1}$  is measured and recorded by the WINDS, but was not available for this study. Use of this high-precision data would have greatly decreased the number of exclusions due to insufficient speed shear between wind layers and permitted more numerous and accurate calculations of roughness length and surface-layer fluxes for all cases. For future work, it is recommended that this high-precision data be acquired. At this level of precision, more careful consideration of flow distortion due to the tower structure would be required. The potential for this distortion to affect the calculations was recognized in this study, but no algorithm for dealing with its effects was developed. Research into the effects of  $z_0$  variability on the exchange and drag coefficients and how these effects should be simulated efficiently in high-resolution numerical models would also be a beneficial study, as would the effect of clouds and precipitation on  $z_0$ .

## APPENDIX. WINDS TOWER LOCATIONS AND INSTRUMENT COMPLEMENTS

Table 1. Locations and instrumentation heights for the four launch critical WINDS towers at CCAFS used in this study. After CSR (2006).

TOWER #	LOCATION	INSTRUMENTATION HEIGHT (m) <sup>1</sup>		
		Wind	Temperature	RH
0002	28° 26' 39" N 80° 33' 44" W	62.2	62.2	62.2
		44.2	-	-
		27.4	-	-
		16.5	16.5	16.5
		3.7	-	-
		-	1.8	1.8
0006	28° 30' 47" N 80° 33' 41" W	62.2	62.2	62.2
		49.4	-	-
		16.5	16.5	16.5
		3.7	-	-
		-	1.8	1.8
0110	28° 34' 11" N 80° 35' 12" W	62.2	62.2	62.2
		49.4	-	-
		16.5	16.5	16.5
		3.7	-	-
		-	1.8	1.8
0313 <sup>2</sup>	28° 37' 32" N 80° 39' 26" W	150.0	150.0	150.0
		120.1	-	-
		89.9	-	-
		62.2	62.2	62.2
		49.4	-	-
		16.5	16.5	16.5
		3.7	-	-
		-	1.8	1.8

<sup>1</sup> Launch critical towers support dual instrumentation packages at each level, aligned northwest to southeast on Towers 0002, 0006, and 0110; and northeast to southwest on Tower 0313.

<sup>2</sup> Tower 0313 also houses redundant Vaisala PTB220 Series barometric pressure sensors at 1.8 m AGL (4.3 m MSL).

Table 2. Locations and instrumentation heights for the 14 safety critical WINDS towers at CCAFS used in this study. After CSR (2006).

TOWER #	LOCATION	INSTRUMENTATION HEIGHT (m)		
		Wind	Temperature	RH
0001	28° 26' 02" N 80° 34' 25" W	16.5 3.7 -	16.5 - 1.8	-
0003	28° 27' 35" N 80° 31' 37" W	16.5 3.7 -	16.5 - 1.8	-
0108	28° 32' 09" N 80° 34' 30" W	16.5 3.7 -	16.5 - 1.8	-
0211	28° 36' 22" N 80° 37' 18" W	16.5 3.7 -	16.5 - 1.8	-
0303	28° 27' 36" N 80° 34' 17" W	16.5 3.7 -	16.5 - 1.86	-
0311	28° 36' 10" N 80° 38' 29" W	16.5 3.7 -	16.5 - 1.8	-
0403	28° 27' 31" N 80° 35' 33" W	16.5 3.7 -	16.5 - 1.8	-
0412	28° 36' 23" N 80° 34' 03" W	16.5 3.7 -	16.5 - 1.8	-
0415	28° 39' 31" N 80° 42' 00" W	16.5 3.7 -	16.5 - 1.8	-
0506	28° 30' 57" N 80° 38' 24" W	16.5 3.7 -	16.5 - 1.8	-
0509	28° 33' 44" N 80° 40' 10" W	16.5 3.7 -	16.5 - 1.8	-
0714	28° 38' 35" N 80° 44' 54" W	16.5 3.7 -	16.5 - 1.8	-
0803	28° 27' 47" N 80° 40' 13" W	16.5 3.7 -	16.5 - 1.8	-
0805	28° 31' 05" N 80° 41' 47" W	16.5 3.7 -	16.5 - 1.8	-

## LIST OF REFERENCES

- Baker, R. D., B. H. Lynn, A. Boone, W.-K. Tao, and J. Simpson, 2001: The influence of soil moisture, coastline curvature, and land-breeze circulations on sea-breeze-initiated precipitation. *J. Hydrometeorol.*, **2**, 193–211.
- Beljaars, A. C. M., and A. A. M. Holtslag, 1991: Flux parameterization over land surfaces for atmospheric models. *J. Appl. Meteorol.*, **30**, 327–341.
- Bohren, C. F., and B. A. Albrecht, 1998: *Atmospheric Thermodynamics*. Oxford Univ. Press, 402 pp.
- Brown, R. A., 1991: *Fluid Mechanics of the Atmosphere*. Academic Press Inc., 489 pp.
- Businger, J. A., J. C. Wyngaard, Y. Izumi, and E. F. Bradley, 1971: Flux-profile relationships in the atmospheric surface layer. *J. Atmos. Sci.*, **28**, 181–189.
- Caton, P. G. F., 1977: Standardised maps of hourly mean wind speed over the U. K. and some implications regarding wind speed profiles. *Proc. 4th Conf. Wind Effects on Buildings and Structures*, Heathrow, 7–21.
- Charnock, H., 1955: Wind stress on a water surface. *Quart. J. Roy. Meteor. Soc.*, **81**, 639–640.
- Computer Sciences Raytheon, 2006: *Eastern Range Instrumentation Handbook*, CDRL A209, Contract F08560-00-C-0005.
- de Rooy, W., and K. Kok, 2004: A combined physical-statistical approach for the downscaling of model wind speed. *Wea. Forecasting*, **19**, 485–495.
- Dyer, A. J., 1974: A review of flux-profile relations. *Bound. Layer Meteor.*, **1**, 363–372.
- Garratt, J. R., 1992: *The Atmospheric Boundary Layer*, Cambridge University Press, 316 pp.
- Holton, J. R., 1992: *An Introduction to Dynamic Meteorology*, Academic Press, 511 pp.
- Jacobs, A. J. M., and N. Maat, 2005: AUTOTREND – Automated guidance for short-term aviation weather forecasts. [Available online at [http://ams.confex.com/ams/11aram22sls/techprogram/paper\\_80750.htm](http://ams.confex.com/ams/11aram22sls/techprogram/paper_80750.htm)] Accessed February 2010.

- Kaimal, J. C., and J. J. Finnigan, 1994: *Atmospheric Boundary Layer Flows: Their Structure and Measurement*, Oxford Univ. Press, 289 pp.
- Kalnay, E., 2003: *Atmospheric Modeling, Data Assimilation and Predictability*, Cambridge Univ. Press, 341 pp.
- Komen, G., P. A. E. M. Janssen, V. Makin, and W. Oost, 1998: On the sea state dependence of the Charnock parameter. *Global Ocean Atmos. Syst.*, **5**, 367–388.
- Laird, N. F., D. A. R. Kristovich, R. M. Rauber, H. T. Ochs III, and L. J. Miller, 1995: The Cape Canaveral sea and river breezes: kinematic structure and convective initiation. *Mon. Wea. Rev.*, **123**, 2942–2956.
- Lenschow, D. H., 1986: *Probing the Atmospheric Boundary Layer*, American Meteorological Society, 269 pp.
- Louis, J. F., 1979: A parametric model of vertical eddy fluxes in the atmosphere. *Bound. Layer Meteor.*, **17**, 187–202.
- Manobianco, J. J., J. W. Zack, and G. E. Taylor, 1996: Workstation-based real-time mesoscale modeling designed for weather support to operations at the Kennedy Space Center and Cape Canaveral Air Station. *Bull. Amer. Meteor. Soc.*, **11**, 653–672.
- McWilliams, J. C., 2006: *Fundamentals of Geophysical Fluid Dynamics*, Cambridge Univ. Press, 249 pp.
- Newton, C. W., 1971: Global angular momentum balance: Earth torques and atmospheric fluxes. *J. Atmos. Sci.*, **28**, 1329–1341.
- Rao, P. A., and H. E. Fuelberg, 2000: An investigation of convection behind the Cape Canaveral sea-breeze front. *Mon. Wea. Rev.*, **128**, 3437–3458.
- Reed, J. W., 1979: Cape Canaveral sea breezes. *J. Appl. Meteorol.*, **18**, 231–235.
- Stewart, R. W., 1979: The atmospheric boundary layer. *Third IMO Lect. 523*, World Meteorol. Org., Geneva.
- Stewart, S. R., and J. L. Beven II, 2009: Tropical cyclone report: Tropical Storm Fay. [Available online at [http://www.nhc.noaa.gov/pdf/TCR-AL062008\\_Fay.pdf](http://www.nhc.noaa.gov/pdf/TCR-AL062008_Fay.pdf)].
- Stull, R. B., 1988: *An Introduction to Boundary Layer Meteorology*, Springer, 670 pp.

- Wakimoto, R. M., and N. T. Atkins, 1994: Observations of the sea-breeze front during CaPE. part I: single-Doppler, satellite, and cloud photogrammetry analysis. *Mon. Wea. Rev.*, **122**, 1092–1114.
- Wang, Q., 2009: *Boundary Layer Meteorology*. Naval Postgraduate School, lecture notes for MR3413.
- Wang, S., Q. Wang, and J. Doyle, 2002: Some improvements to Louis flux parameterization. [Available online at <http://ams.confex.com/ams/pdfpapers/44519.pdf>] Accessed March 2010.
- Wieringa, J., 1976: An objective exposure correction method for average wind speeds measured at a sheltered location. *Quart. J. Roy. Meteor. Soc.*, **102**, 241–253.
- , 1986: Roughness-dependent geographical interpolation of surface wind speed averages. *Quart. J. Roy. Meteor. Soc.*, **112**, 867–889.

THIS PAGE INTENTIONALLY LEFT BLANK

## INITIAL DISTRIBUTION LIST

1. Defense Technical Information Center  
Ft. Belvoir, Virginia
2. Dudley Knox Library  
Naval Postgraduate School  
Monterey, California
3. Professor Qing Wang  
Naval Postgraduate School  
Monterey, California
4. Professor Wendell A. Nuss  
Naval Postgraduate School  
Monterey, California
5. Air Force Weather Technical Library  
Asheville, North Carolina